

Lubrication in a corner

Roman Stocker and A. E. Hosoi

August 24, 2004
HML Report Number 04-P-03

Lubrication in a corner

By ROMAN STOCKER¹ AND A. E. HOSOI²

¹Department of Mathematics, Massachusetts Institute of Technology, 77 Massachusetts Avenue, Cambridge, MA 02139, USA, stocker@math.mit.edu

²Department of Mechanical Engineering, Hatsopoulos Microfluidics Laboratory, Massachusetts Institute of Technology, 77 Massachusetts Avenue, Cambridge, MA 02139, USA, peko@mit.edu

(Received ?? and in revised form ??)

A mathematical model for the evolution of a thin film in an interior corner region is presented. The model is based on the idea that the film can be considered thin everywhere in the η direction if viewed in the new coordinate system ($\xi = x^2 - y^2$, $\eta = 2xy$). Lubrication theory is applied to the governing equations written in this coordinate system. The exact integration of the mass conservation equation for a no-slip boundary condition yields a single evolution equation, which is integrated numerically. The evolution of a thin film driven by surface tension and gravity is predicted as a function of the Bond number and successfully compared to laboratory experiments.

1. Introduction

Thin liquid films are a topic of considerable interest due to their wide range of practical applications and to the availability of reduced models to investigate their behaviour. These films are important in industry, where they are used to coat and protect surfaces, for example autobodies and beverage containers (Roy, Roberts & Simpson 2002), or as paints, adhesives and membranes. Biophysical applications include the liquid lining of the lungs (Grotberg 1994), where capillary-elastic instabilities can lead to collapse of a vessel (Rosenzweig & Jensen 2002), the film protecting the cornea of the eye (Wong, Fatt & Radke 1996) and the motion of contact lenses (Moriarty & Terrill 1996). In environmental processes, thin films appear in foam dynamics (Wasan, Koczo & Nikolov 1994), lava flows or gravity currents under water (Huppert 1982), and the transport of bacteria in laminar flow over soil (Myers 2003). In agriculture, they play an important role in determining the effectiveness of agrochemicals like insecticides and herbicides (Schwartz & Weidner 1995). Thin films can exhibit very rich dynamics, including wave propagation, steepening, and fingering. The possibility of rupture is discussed by Bertozzi & Pugh (1998), who used energy methods to determine when a general class of thin film equations can develop finite-time singularities. The effects of Van der Waals forces and surfactants were investigated by Ida & Miksis (1998*a,b*). The extensive literature on these topics is reviewed in Oron, Davis & Bankoff (1997) and Myers (1998).

When the dominant gradients in the flow variables occur *across* the film thickness — as for example in a film over a solid substrate — shear stresses dominate over extensional stresses and the appropriate reduced models are known as lubrication (or thin-film) models. If, on the other hand, gradients *along* the film prevail — as in free films such as foams — reduced models are referred to as slender-body (or slender-rod, or thin-filament) models. Both of these cases are examples of long-wavelength approximations. Here we will develop a lubrication model for corner flows bounded by a substrate. These reduced models rely on the existence of two widely disparate length scales. By assuming that

the slope of the free surface is small, the full governing equations can be reduced to one or two nonlinear evolution equations. These are then easily solved numerically. The advantages over an entirely numerical approach include avoiding the complexity of the original free-boundary problem, computational savings and a deeper understanding of the underlying physics.

Recently, considerable attention has been devoted to thin film flows over topography. In the coating of microelectronic components, for example, one aims to reduce the inside ('fat edges') and outside ('picture framing') corner defects (Schwartz & Weidner 1995). The shape of the interface is dictated by the competition between the substrate, which impresses its shape onto that of the interface — effectively contributing an additional capillary pressure — and surface tension, tending to flatten the free surface and to drive the solution to stable minimum-energy configurations (Kalliadasis, Bielarz & Homsy 2000). Short-wavelength irregularities of the free surface are rapidly levelled by surface tension forces, while the long-term evolution is determined primarily by the topography of the substrate (Roy *et al.* 2002).

Unfortunately, due to the small-slope assumption, a standard lubrication approach is *a priori* not expected to be accurate near the edges of steep features. Despite this limitation Stillwagon & Larson (1988, 1990) derived, and successfully compared to experiments, a single fourth-order, nonlinear, diffusion-like evolution equation describing the levelling of micron-sized isolated trenches by spin-coating under the action of surface tension. Kalliadasis *et al.* (2000) extended lubrication theory over topography to include an external body force, such as gravity, and found that the free surface develops a ridge just before the entrance to a trench, due to the capillary pressure gradient induced by the curvature of the substrate. Schwartz & Weidner (1995) took a different approach and adopted a local orthogonal coordinate system that naturally fits an arbitrarily curved substrate where the film thickness is assumed to be small compared to the radius of curvature of the substrate. Roy *et al.* (2002) developed a more complex method, in which an artificial variable, proportional to the amount of liquid locally above the substrate, is used instead of the liquid thickness and gravity and inertia are included *a posteriori* via centre manifold techniques. The latter two studies are both based on the same assumptions as Stillwagon & Larson (1988) and no attempt is made at modelling sharp features such as a corner.

The evolution equation used by Stillwagon & Larson (1988, 1990) and Kalliadasis *et al.* (2000) assumes that the slopes of both the free surface and the substrate are small (Kalliadasis *et al.* 2000). The lubrication approximation is formally valid only for small-slope profiles and small Capillary numbers (Mazouchi & Homsy 2001) and is expected to break down in the immediate vicinity of a sharp step (Kalliadasis *et al.* 2000). In this case, the full Stokes equations are appropriate. Mazouchi & Homsy (2001) investigated free surface Stokes flow over topography with sharp edges using a boundary integral method, finding good agreement with lubrication theory for small Capillary numbers even for steep features. This indicates that the area around the sharp step where lubrication breaks down is small and does not significantly affect the levelling of the trench, validating results by Stillwagon & Larson (1990) and Kalliadasis *et al.* (2000).

On the other hand, there are many cases in which the dominant physics occurs inside the corner region, as sketched in figure 1 (*a*). For these, the above approaches fail because large gradients of the free surface develop and the slope cannot be small everywhere. Furthermore, the curvature of the substrate diverges at the corner. We propose a model that relies on a change of coordinates to address this gap in the thin film approximation. We then develop the lubrication approximation — based on this change of coordinates

— for a film bounded by a solid corner. In Stocker & Hosoi (2004) we make use of the same coordinate system to develop a slender-body model for free corner films.

An example of a film evolving in a corner bounded by two solid walls is the flow of long gas bubbles in square or rectangular capillaries (Kolb & Cerro 1993*a,b*; Thulasidas, Abraham & Cerro 1995; Bico & Queré 2002; Hazel & Heil 2002), sketched in figure 1 (*c*). This mechanism has important applications in oil recovery from porous rocks, in the coating of tubes of square cross-section and in automotive or industrial monolithic reactors. For oil recovery, square capillaries provide a better model for the irregular and angular nature of the porous media and the thickness of the wetting film is a direct measure of the unrecoverable oil fraction (Kolb & Cerro 1993*b*). Liquid corner regions arise also in the imbibition of a close-packed assembly of fibers (Bico & Queré 2002). Weislogel & Lichter (1998) and Weislogel (2001) investigated capillary flow in an interior corner by looking at the evolution of the flow in a direction perpendicular to the plane of the corner. Theoretical analysis has been developed for axisymmetric bubbles (Kolb & Cerro 1993*a,b*; Thulasidas *et al.* 1995). The bubbles are axisymmetric when the Capillary number is larger than 0.04 (Thulasidas *et al.* 1995). For smaller values, bubbles become non-axisymmetric and flatten out against the tube walls, creating liquid regions in the corners separated by thin flat films (figure 1*c*). In the reference frame of the bubble, the flow in these corner regions (sufficiently far away from both ends of the bubble) is an example of a thin film in a corner. The lubrication approximation is appropriate for this wall-bounded flow configuration.

An example of a free film in a corner is a coarsening foam (figure 1*b*). Foams — whose evolution and breakup are as yet poorly understood — are important in a wide range of applications, such as food and chemical industries, fire-fighting and structural material science (Hilgenfeldt, Koehler & Stone 2001). Here a symmetry boundary condition is required at the corner’s sides, qualifying this as a slender-body system. As this problem is treated in more detail in Stocker & Hosoi (2004), we will only briefly address the relevance of our change of coordinates to this case in the Discussion section.

The application of the proposed change of coordinates that originally motivated the present work is the ‘fishbone’ instability observed in filament stretching experiments (sketched in figure 1*d*) performed on polystyrene-based Boger fluids by Spiegelberg & McKinley (1996). This instability occurs exactly at the corner formed by two orthogonally intersecting thin films (figure 10*b* of Spiegelberg & McKinley 1996). A mechanistic explanation of this instability would contribute to the understanding of non-Newtonian free surface flows.

In the configuration we are considering the film is thin along both walls (figure 1*a*), in contrast to the classical Landau-Levich problem (Landau & Levich 1942), where an infinite plate is pulled out from a deep pool of liquid. Landau and Levich derived separate expressions for the thin film coating the plate and the meniscus in the deep pool and closed the problem by matching curvatures. This approach differs from ours in two important respects. First, the deep pool is replaced by a thin film in which viscous stresses dominate. Second, the weakest point in the Landau-Levich solution — the matching — occurs precisely in the region of interest, the corner. This prompted us to look for a different model, and eventually to develop the change of coordinates described in this work.

After deriving the governing equations in the new coordinate system in the next section, lubrication theory is applied in § 3 to derive an evolution equation for a film with no-slip boundaries. Details of the derivations are presented in two appendices. The numerical method applied in solving the evolution equation is detailed in § 4 and results are given in § 5. We chose not to perform a transverse linear stability analysis, since our focus in

this paper is to present a method to develop lubrication theory in a corner and not on the physical mechanism responsible for instability in any particular context. Comparisons with experiments, designed to provide a test bed for the model, are presented in § 6. The final section discusses the limitations of the model and the modifications required for several applications.

2. Hyperbolic coordinates

2.1. The governing equations in vector form

The flow in an interior corner is considered, as sketched in figure 1 (a). The momentum and continuity equations are, respectively,

$$0 = -\frac{\nabla p}{\rho} + \nu \nabla^2 \mathbf{u} - g \hat{\mathbf{k}}, \quad \nabla \cdot \mathbf{u} = 0, \quad (2.1a, b)$$

where \mathbf{u} is the velocity field, p is the pressure, ν is the kinematic viscosity, ρ is the density, g is the acceleration of gravity and $\hat{\mathbf{k}}$ is the unit vertical vector, positive upwards. Since this work is concerned with low Reynolds number flows, inertia terms have been neglected in (2.1). We will consider two-dimensional systems, assuming no variation in the third dimension. The two stress boundary conditions at the free surface are

$$\hat{\mathbf{n}} \cdot \mathbf{\Pi} \cdot \hat{\mathbf{n}} = \sigma \kappa, \quad \hat{\mathbf{t}} \cdot \mathbf{\Pi} \cdot \hat{\mathbf{n}} = 0, \quad (2.2a, b)$$

where $\hat{\mathbf{n}}$ and $\hat{\mathbf{t}}$ are the unit outward normal and tangent vectors to the free surface, respectively, σ is the surface tension, and $\kappa = -\nabla \cdot \hat{\mathbf{n}}$ is the curvature of the free surface. For a Newtonian fluid, the stress tensor is

$$\mathbf{\Pi} = \mu [\nabla \mathbf{u} + (\nabla \mathbf{u})^T] - p \mathbf{I}, \quad (2.3)$$

where $\mu = \rho \nu$ is the dynamic viscosity, \mathbf{I} the identity matrix and T indicates a transpose matrix. Furthermore, conservation of mass and no-slip at the corner's walls will be imposed.

2.2. The change of coordinates

The fundamental idea presented herein is to exploit the fact that the film is thin everywhere along the wall. This will allow us to apply lubrication theory to reduce the governing equations to a single evolution equation. Cartesian coordinates (x, y) are not well suited for such an approximation, because the film is not everywhere thin in one of the two coordinate directions (or, equivalently, because the slope is not everywhere small). On the other hand, if we introduce the hyperbolic coordinate system

$$\xi = x^2 - y^2, \quad \eta = 2xy, \quad (2.4a, b)$$

shown in figure 2, the film can be treated as thin everywhere in the η direction. Note that the Cartesian axes now correspond to $\eta = 0$, with η increasing with x and y in the first quadrant (we are not interested in the remaining quadrants). The second coordinate, ξ , increases along the wall from large y towards large x , in the shape of hyperbolas. The change of coordinates (2.4) is a special case ($n = 2$) of the analytical conformal map transformation for a corner of angle π/n :

$$\xi = \text{Re}[(x + iy)^n], \quad \eta = \text{Im}[(x + iy)^n], \quad (2.5a, b)$$

where Re and Im indicate the real and imaginary part, respectively. The derivations become cumbersome for arbitrary n . Here we will pursue the simplest and most interesting case of a square corner ($n = 2$).

The coordinate system (2.4) is orthogonal, since the mixed scale factor

$$\frac{\partial x}{\partial \xi} \frac{\partial x}{\partial \eta} + \frac{\partial y}{\partial \xi} \frac{\partial y}{\partial \eta} \quad (2.6)$$

is everywhere zero. The scale factors associated with the ξ and η directions are equal and given by

$$s = \left[\left(\frac{\partial x}{\partial \xi} \right)^2 + \left(\frac{\partial y}{\partial \xi} \right)^2 \right]^{1/2} = \left[\left(\frac{\partial x}{\partial \eta} \right)^2 + \left(\frac{\partial y}{\partial \eta} \right)^2 \right]^{1/2} = \frac{1}{2\sqrt{r}}, \quad (2.7)$$

where $r = (\xi^2 + \eta^2)^{1/2} = x^2 + y^2$. The derivatives of (x, y) with respect to (ξ, η) — as well as the expressions for gradient, divergence and Laplacian in hyperbolic coordinates — are given in appendix A.1. The coordinate transformation (2.4) is singular at the origin. However, this does not represent a problem since — excluding rupture at the origin — the free surface of the film never passes through the singularity.

2.3. The governing equations in the hyperbolic coordinates

Using (A 1), (A 2), (A 4), and (A 12), we can rewrite the governing equations (2.1) in the hyperbolic coordinates:

$$\frac{\partial u}{\partial \xi} + \frac{\partial v}{\partial \eta} + f_1 u + f_2 v = 0, \quad (2.8a)$$

$$\frac{1}{\rho} \frac{\partial p}{\partial \xi} = \frac{\nu}{s} \left[\frac{\partial^2 u}{\partial \xi^2} + \frac{\partial^2 u}{\partial \eta^2} - \frac{1}{r^2} \left(\eta \frac{\partial v}{\partial \xi} - \xi \frac{\partial v}{\partial \eta} + \frac{u}{4} \right) \right] - g \frac{\partial y}{\partial \xi}, \quad (2.8b)$$

$$\frac{1}{\rho} \frac{\partial p}{\partial \eta} = \frac{\nu}{s} \left[\frac{\partial^2 v}{\partial \xi^2} + \frac{\partial^2 v}{\partial \eta^2} - \frac{1}{r^2} \left(-\eta \frac{\partial u}{\partial \xi} + \xi \frac{\partial u}{\partial \eta} + \frac{v}{4} \right) \right] - g \frac{\partial y}{\partial \eta}, \quad (2.8c)$$

where f_1 , f_2 , $\partial y / \partial \xi$ and $\partial y / \partial \eta$ are functions only of the position (ξ, η) and are defined in appendix A.1. The explicit dependence of the equations on position represents a difference with respect to Cartesian coordinates. The first two terms in the square brackets are the Laplacian of the scalar quantities u and v , while the remaining terms arise because the unit vectors $\hat{\xi}$ and $\hat{\eta}$ are position dependent (see appendix A.2).

In order to transform the normal stress boundary condition (2.2a), the curvature κ in the new coordinates is computed from the unit outward normal vector (A 5) using (A 2b):

$$\kappa = -\nabla \cdot \hat{\mathbf{n}} = \frac{h''}{s(1+h'^2)^{3/2}} + \frac{h'f_1 - f_2}{s(1+h'^2)^{1/2}}. \quad (2.9)$$

Using the expression for a Newtonian stress tensor (A 7) together with (A 5), (A 6), and (2.9), allows us to write the stress boundary conditions (2.2) as

$$\begin{aligned} -p + \frac{2\mu}{s(1+h'^2)} \left[\frac{\partial v}{\partial \eta} - \frac{\xi u}{2r^2} + h'^2 \left(\frac{\partial u}{\partial \xi} - \frac{\eta v}{2r^2} \right) + \right. \\ \left. -h' \left(\frac{\partial v}{\partial \xi} + \frac{\partial u}{\partial \eta} + \frac{\eta u + \xi v}{2r^2} \right) \right] = \sigma \kappa, \end{aligned} \quad (2.10a)$$

$$2h' \left(\frac{\partial v}{\partial \eta} - \frac{\partial u}{\partial \xi} + \frac{\eta v - \xi u}{2r^2} \right) + (1 - h'^2) \left(\frac{\partial v}{\partial \xi} + \frac{\partial u}{\partial \eta} + \frac{\eta u + \xi v}{2r^2} \right) = 0. \quad (2.10b)$$

The last equation to be imposed is conservation of mass (or, equivalently, volume, since we assume a constant density), expressing the fact that the time rate of change of a volume element must equal the net volume flux entering from the neighboring elements.

In (ξ, η) the volume of liquid between ξ and $\xi + \Delta\xi$ is

$$\int_0^{h(\xi)} \int_{\xi}^{\xi+\Delta\xi} s^2 d\xi d\eta = \Delta\xi \int_0^{h(\xi)} s^2 d\eta, \quad (2.11)$$

where we used the fact that a volume element can be approximated as a rectangle of width $s\Delta\xi$ as $\Delta\xi \rightarrow 0$. The net flux into the element is

$$\int_0^{h(\xi)} u(\xi, \eta) s d\eta - \int_0^{h(\xi+\Delta\xi)} u(\xi + \Delta\xi, \eta) s d\eta. \quad (2.12)$$

As $\Delta\xi \rightarrow 0$, mass conservation therefore implies

$$\frac{\partial A}{\partial t} + \frac{\partial Q}{\partial \xi} = 0, \quad (2.13)$$

where

$$A = \int_0^{h(\xi)} s^2 d\eta, \quad Q = \int_0^{h(\xi)} u(\xi, \eta) s d\eta. \quad (2.14a, b)$$

As we will see, the integrals (2.14) can be solved analytically for the lowest order velocity profile $u(\xi, \eta)$ resulting from the lubrication approximation, allowing mass conservation to be satisfied exactly. In the next section, lubrication theory is applied to the full governing equations (2.8), (2.10), and (2.13) to obtain a single evolution equation for the film thickness $h(\xi, t)$.

3. Lubrication theory

3.1. The reduced equations

In this section we derive the evolution equation for a thin layer of liquid evolving under gravity and surface tension in a corner when a no-slip boundary condition is imposed at $\eta = 0$, the two walls bounding the corner. We first rescale the governing equations (2.8), (2.10) and (2.13) by writing

$$\xi = L\tilde{\xi}, \quad u = \mathcal{U}\tilde{u}, \quad t = T\tilde{t} = \sqrt{L}t/\mathcal{U}, \quad (3.1a-c)$$

$$\eta = H\tilde{\eta}, \quad v = \mathcal{V}\tilde{v}, \quad p = P\tilde{p}, \quad (3.1d-f)$$

where tildes denote dimensionless variables. Here L is the (square of the) characteristic long dimension of the layer, H is a scale representing the product of the characteristic transverse dimension and the characteristic long dimension (because $\eta = 2xy$), \mathcal{U} and \mathcal{V} are characteristic velocities along and across the layer, respectively, and P is the pressure scale. Since ξ and η are quadratic in the original coordinates (x, y) , L and H have the dimensions of a length squared, and represent the characteristic ‘length’ and ‘thickness’ of the film in the new coordinate system. In order to include the case of zero gravity, a characteristic velocity along the wall is defined in terms of viscosity and surface tension as $\mathcal{U} = \sigma/\mu$. Thus, the characteristic time $T = \sqrt{L}/\mathcal{U}$ required for a fluid parcel with velocity \mathcal{U} to travel the physical length \sqrt{L} of the layer, becomes $T = \mu\sqrt{L}/\sigma$. Since only dimensionless variables will be used from now on unless otherwise stated, the tildes will be dropped.

In the lubrication limit, it is natural to assume the parameter $\epsilon = H/L$ as small and

to expand the dependent variables u , v and p in powers of ϵ :

$$u = u_0 + \epsilon^2 u_2 + O(\epsilon^4), \quad (3.2a)$$

$$v = v_0 + \epsilon^2 v_2 + O(\epsilon^4), \quad (3.2b)$$

$$p = p_0 + \epsilon^2 p_2 + O(\epsilon^4). \quad (3.2c)$$

The expansion parameter ϵ is proportional to the filling fraction, the detailed relation depending on the initial condition. Quantities depending on the position (ξ, η) are also made dimensionless (f_1 scales like L , f_2 like ϵ/L , and s like $1/\sqrt{L}$). We rescale (2.8), (2.10), and (2.13), substitute for (3.2), and retain only the lowest order terms in ϵ . The position-dependent terms f_1 , f_2 , and s also involve the expansion parameter ϵ and could in principle be expanded in powers of ϵ . However, this makes the equations singular at $\xi = 0$. Further details on this point are given in §3.3, where we discuss an approximated solution, derived by retaining only the leading order terms for the position-dependent quantities.

The continuity equation (2.8a) yields a relation between the two velocity scales, $\mathcal{V} = \epsilon \mathcal{U}$. The Bond number $Bo = \rho g L / \sigma$ represents the relative importance of gravity and surface tension. The momentum equation along ξ (2.8b) suggests a pressure scale $P = \sigma / (\epsilon^2 \sqrt{L})$, which is standard for lubrication theory (Myers 2003), and thus reduces to

$$\frac{\partial p_0}{\partial \xi} = 2 (\xi^2 + \epsilon^2 \eta^2)^{1/4} \frac{\partial^2 u_0}{\partial \eta^2} - \epsilon^2 Bo \frac{\partial y}{\partial \xi}, \quad (3.3)$$

where $\partial y / \partial \xi$ is a function of position only, given in (A 1c). The momentum equation along η (2.8c) becomes

$$\frac{\partial p_0}{\partial \eta} = -\epsilon^2 Bo \frac{\partial y}{\partial \eta}, \quad (3.4)$$

while the stress boundary conditions are

$$-p_0 = \epsilon^3 \kappa, \quad \frac{\partial u_0}{\partial \eta} = 0 \quad (\eta = h). \quad (3.5a, b)$$

In (3.3), (3.4) and (3.5) we chose to retain gravity and surface tension to leading order, since we are interested in the case in which both effects enter the dominant balance. In particular, we have retained the full curvature in (3.5a), as done first by Ruschak (1978). This ensures that the potential energy is the same as that of the full equations, so that ‘exact surfaces of static equilibrium are also equilibrium solutions of the model’ (Eggers & Dupont 1994), these being the states that minimize potential energy.

3.2. The evolution equation

The system of equations at $O(1)$, namely (2.13), (3.3), (3.4), and (3.5) can now be solved subject to the no-slip boundary condition. Integrating (3.4) in η , from η to h , and imposing the normal stress boundary condition (3.5a) at $\eta = h$, yields an expression for pressure:

$$p_0 = -\epsilon^3 \kappa + \epsilon^2 Bo \left[y \Big|_h - y \Big|_\eta \right], \quad (3.6)$$

where y is given in terms of ξ and η in (A 1a) and the vertical bar indicates at which value of η a quantity is evaluated. Substituting (3.6) into (3.3) and rearranging, we find

$$\frac{\partial^2 u_0}{\partial \eta^2} = \frac{\epsilon^2 g_2(\xi)}{2 (\xi^2 + \epsilon^2 \eta^2)^{1/4}}, \quad (3.7)$$

where

$$g_2(\xi) = -\epsilon\kappa' + Bo \frac{\partial y}{\partial \xi} \Big|_h. \quad (3.8)$$

The curvature gradient κ' is obtained after some algebra as

$$\kappa' = \frac{2\alpha}{\beta^3} h''' - \frac{6\epsilon^2\alpha}{\beta^5} h' (h'')^2 - \frac{3(h - \xi h')(\xi + \epsilon^2 h h')}{2\alpha^7 \beta}, \quad (3.9)$$

where $\alpha = (\xi^2 + \epsilon^2 h^2)^{1/4}$ and $\beta = (1 + \epsilon^2 h'^2)^{1/2}$, and

$$\frac{\partial y}{\partial \xi} \Big|_h = \frac{1}{2\sqrt{2} \left(\sqrt{\xi^2 + \epsilon^2 h^2} - \xi \right)^{1/2}} \left[\frac{\xi + \epsilon^2 h h'}{\sqrt{\xi^2 + \epsilon^2 h^2}} - 1 \right]. \quad (3.10)$$

Again, we will not approximate the latter expression to avoid incurring singularities at $\xi = 0$.

The integration of (3.7) can be carried out exactly in terms of the hypergeometric functions ${}_2F_1$ (e.g. Abramowitz & Stegun 1965). Making use of (3.5b) and the no-slip condition $u_0 = 0$ at $\eta = 0$, we eventually find

$$u_0(\eta, \xi) = \frac{g_2(\xi)|\xi|^{3/2}}{3} \left[1 - {}_2F_1 \left(-\frac{1}{2}, -\frac{3}{4}; \frac{1}{2}; -\frac{\epsilon^2 \eta^2}{\xi^2} \right) - \frac{3\epsilon^2 \eta h}{2\xi^2} {}_2F_1 \left(\frac{1}{4}, \frac{1}{2}; \frac{3}{2}; -\frac{\epsilon^2 h^2}{\xi^2} \right) \right]. \quad (3.11)$$

Note that the first hypergeometric function is evaluated at η , while the second one is evaluated at h . As shown in §5, this velocity profile differs slightly from the parabolic profile expected for unidirectional lubrication theory, a consequence of the fact that the film has to negotiate the corner.

When we substitute (3.11) into the mass conservation equation (2.13), all integrals except for one can be evaluated exactly. In particular:

$$\begin{aligned} \frac{\partial}{\partial t} \int_0^{h(\xi)} s^2 d\eta &= \frac{\partial}{\partial t} \int_0^{h(\xi)} \frac{1}{4(\xi^2 + \epsilon^2 \eta^2)^{1/2}} d\eta = \frac{\partial}{\partial t} \left[\frac{\ln(2\epsilon h + 2(\xi^2 + \epsilon^2 h^2)^{1/2}) - \ln(2|\xi|)}{4\epsilon} \right] \\ &= \frac{1}{4(\xi^2 + \epsilon^2 h^2)^{1/2}} \frac{\partial h}{\partial t}. \end{aligned} \quad (3.12)$$

In addition, the following two indefinite integrals are used:

$$\int \frac{1}{(\xi^2 + \epsilon^2 \eta^2)^{1/4}} d\eta = \frac{h}{|\xi|^{1/2}} {}_2F_1 \left(\frac{1}{4}, \frac{1}{2}; \frac{3}{2}; -\frac{\epsilon^2 \eta^2}{\xi^2} \right), \quad (3.13a)$$

$$\int \frac{\eta}{(\xi^2 + \epsilon^2 \eta^2)^{1/4}} d\eta = \frac{2}{3\epsilon^2} (\xi^2 + \epsilon^2 \eta^2)^{3/4}. \quad (3.13b)$$

The evolution equation for the film thickness eventually is found to be:

$$\frac{1}{4(\xi^2 + \epsilon^2 h^2)^{1/2}} \frac{\partial h}{\partial t} - \frac{\epsilon}{6} \frac{\partial}{\partial \xi} \left\{ h^2 g_2(\xi) R \left(\frac{\xi}{\epsilon h} \right) \right\} = 0, \quad (3.14)$$

where

$$R(z) = |z| \left\{ \left[-2 + \left(1 + \frac{1}{z^2} \right)^{3/4} \right] {}_2F_1 \left(\frac{1}{4}, \frac{1}{2}; \frac{3}{2}; -\frac{1}{z^2} \right) + \int_0^1 \frac{{}_2F_1 \left(-\frac{1}{2}, -\frac{3}{4}; \frac{1}{2}; -\frac{\hat{\eta}^2}{z^2} \right)}{(1 + \hat{\eta}^2/z^2)^{1/4}} d\hat{\eta} \right\}. \quad (3.15)$$

We were unable to evaluate the last integral analytically. The evolution equation (3.14) is a fourth order, nonlinear, partial differential equation for the film thickness $h(\xi, t)$.

In a unidirectional lubrication theory that uses arclength along the substrate as the long coordinate (e.g. Schwartz & Weidner 1995; Roy *et al.* 2002), the second derivative of the substrate's curvature (a delta function) enters the evolution equation. This represents a strong singularity and cannot be handled numerically without approximations. By adopting our change of coordinates, the only remnant of the substrate's sharp corner is a weak singularity in (3.14) arising from the absolute value in (3.15). Assuming that the gradient of the free-surface curvature κ' ($\approx h'''$) can offset the discontinuity, it can be shown that h is at least C^2 , that is the singularity shows up only in the third and higher derivatives. This weak discontinuity is easily overcome by the numerical solution, as demonstrated in what follows by the smoothness of all our numerical profiles. In the next section we discuss an approximation to (3.14).

3.3. An approximation of the evolution equation

The price to pay for avoiding singularities due to the sharp corner, is that we must retain ϵ in the final evolution equation (or, alternatively, in the initial condition). In most formulations, albeit not all (e.g. Hosoi & Mahadevan 1999), this does not occur. The reason for retaining ϵ in the position-dependent terms is that lubrication theory is based on the relative magnitude of variations in the dependent variables, that is derivatives. No assumptions are made about quantities that depend on position alone. This is a non-issue in Cartesian coordinates, as purely position-dependent terms never arise. While one may not call our approach 'standard lubrication theory' due to this perhaps spurious retention of the expansion parameter ϵ , it is nevertheless clear that our formulation provides a straightforward way of dealing with a geometry that is taboo for most other methods, without resorting to the full Stokes equations. For this reason, the filling fraction remains as a parameter, through ϵ .

In this paper, all integrals in the mass conservation equation but one could be solved exactly. On the other hand, it is to be expected that in more complex scenarios — such as a domain stretching in time or a non-Newtonian stress tensor — those integrals cannot be solved exactly. The approximation of the position-dependent terms would then possibly allow an exact integration. It is therefore important to have an understanding of the accuracy of this approximation. In this section we derive an approximated evolution equation obtained by expanding the position-dependent terms in ϵ . In the present case the only such term is $1/s$ in (2.8b), which reduces to

$$\frac{1}{s} = 2(\xi^2 + \epsilon^2 \eta^2)^{1/4} \approx 2|\xi|^{1/2} \left[1 + O\left(\frac{\epsilon \eta}{\xi}\right)^2 \right]. \quad (3.16)$$

The only difference introduced by the approximation in (3.16) in the governing equations is that $|\xi|^{1/2}$ replaces $(\xi^2 + \epsilon^2 \eta^2)^{1/4}$ in (3.3), yielding

$$\frac{\partial^2 u_0}{\partial \eta^2} = \frac{\epsilon^2 g_2(\xi)}{2|\xi|^{1/2}} \quad (3.17)$$

instead of (3.7). The right-hand-side of (3.17) is now independent of η , allowing two straightforward integrations in η . Use of the boundary conditions at $\eta = 0$ and h yields

$$u_0 = \frac{\epsilon^2 g_2(\xi)}{2|\xi|^{1/2}} \left(\frac{\eta^2}{2} - \eta h \right), \quad (3.18)$$

recovering the typical parabolic velocity profile of lubrication theory. When this expression is substituted into the mass conservation equation (2.13), the following integrals

arise:

$$\frac{1}{2} \int_0^{h(\xi)} \eta^2 s d\eta = \frac{h}{10\epsilon^2} \left[(\xi^2 + \epsilon^2 h^2)^{3/4} - |\xi|^{3/2} {}_2F_1 \left(\frac{1}{2}, \frac{1}{4}; \frac{3}{2}; -\frac{\epsilon^2 h^2}{\xi^2} \right) \right], \quad (3.19a)$$

$$\int_0^{h(\xi)} \eta h s d\eta = \frac{h}{2} \int_0^{h(\xi)} \frac{\eta}{(\xi^2 + \epsilon^2 \eta^2)^{1/4}} d\eta = \frac{h}{3\epsilon^2} \left[(\xi^2 + \epsilon^2 h^2)^{3/4} - |\xi|^{3/2} \right] \quad (3.19b)$$

We eventually find the approximated evolution equation to be of the same form as (3.14), with $R(z)$ in (3.15) replaced by

$$R_{approx}(z) = |z| \left[-1 + \frac{7}{10} \left(1 + \frac{1}{z^2} \right)^{3/4} + \frac{3}{10} {}_2F_1 \left(\frac{1}{4}, \frac{1}{2}; \frac{3}{2}; -\frac{1}{z^2} \right) \right]. \quad (3.20)$$

In order to confidently use this approximation, we need to quantify the error we are introducing. It is evident that $R_{approx} \rightarrow R$ (3.15) when $|z| \gg 1$ (i.e. $|\xi| \gg \epsilon h$, as $z = \xi/(\epsilon h)$). However, as $z \rightarrow 0$, $R(z) \rightarrow 1$ while $R_{approx}(z)$ diverges, indicating that in general R_{approx} is not a good representation of R close to $\xi = 0$. This is shown in figure 3(a), where the ratio R_{approx}/R is plotted for three values of ϵ and $h = 1$. In computing $R(z)$, the integral in (3.15) was evaluated numerically using the trapezoidal rule with 20 intervals for $\hat{\eta}$. The ratio R_{approx}/R always diverges as $\xi \rightarrow 0$, but it asymptotes to 1 as $\xi \rightarrow \infty$ in all three cases, showing that R_{approx} is a good approximation for R for all values of ξ , except for the region closest to zero. The discrepancy is barely discernible in figure 3(a) for $\epsilon = 0.001$, but grows with ϵ . On the other hand, we can show that the influence of this region is small. Figure 3(b) shows that the error incurred by approximating R by R_{approx} tends to zero as $\epsilon \rightarrow 0$. That error was computed as the integral of $R_{approx}/R - 1$ over $0 < \xi \leq 1$. Since $R_{approx} \rightarrow \infty$ as $|\xi| \rightarrow 0$, we started the numerical integration at $\xi = 10^{-5}$ and verified that the changes induced by a smaller starting value are negligible. The error grows approximately like $\epsilon^{0.9}$. Thus, the integral contribution of the point-wise singularity to the overall evolution of the film is subdominant (mathematically, a portion of the integrand diverges, but its contribution to the integral is nevertheless small) and we can expect accurate results for thin films even when the position-dependent terms are approximated. Such an approximated solution is effectively equivalent to solving left and right of $\xi = 0$ and then arguing that — as the approximation breaks down only in a tiny neighborhood of $\xi = 0$ — any errors that may be introduced are bounded owing to exact mass conservation.

As the approximation (3.20) involves no significant loss in accuracy, but considerable saving in computational time (due to elimination of the integral to be evaluated numerically in (3.15)), all results in this paper are based on the approximated solution. The fact that the outcomes agree well with both theoretical and experimental results — as will be seen — justifies this procedure. In particular, no singular behaviour near $\xi = 0$ was observed in any of the simulations. In the next section we describe the numerical scheme we used to solve (3.14) with $R(z)$ given by (3.20).

4. Numerical solution of the evolution equation

In our numerical solution the fourth order equation (3.14) is first split into two second order equations, by defining an auxiliary variable $f = h''$ (which is not the curvature, since we are not in Cartesian coordinates). Denoting the term in curly brackets in (3.14)

as q , the numerical scheme becomes

$$F_i^{n+1} = \frac{1}{[\xi_i^2 + \epsilon^2(h_i^{n+1})^2]^{1/2}} \frac{h_i^{n+1} - h_i^n}{\Delta t} - \frac{\epsilon}{6} \frac{(q_{i+1/2}^{n+1} - q_{i-1/2}^{n+1})}{(\Delta_i^+ - \Delta_i^-)/2} = 0, \quad (4.1a)$$

$$G_i^{n+1} = f_i^{n+1} - m_i^+ h_{i+1}^{n+1} - m_i h_i^{n+1} - m_i^- h_{i-1}^{n+1} = 0, \quad (4.1b)$$

where subscript i represents the i th grid point, and the free surface is located at (ξ_i, h_i^{n+1}) at time step $n+1$. The integration was performed on a non-uniform grid, so that a higher grid-point density could be adopted closest to the corner. Details of the grid are given in appendix B. The distance between grid point i and its two neighbors $i \pm 1$ is $\Delta_i^\pm = |\xi_{i\pm 1} - \xi_i|$. First derivatives were approximated by centered differences. Second derivatives were computed on a three point stencil as a weighted average of the first forward and backward derivatives, as in (4.1b), with $m_i^+ = 2/[\Delta_i^+(\Delta_i^+ + \Delta_i^-)]$, $m_i = -2/(\Delta_i^+ \Delta_i^-)$ and $m_i^- = 2/[\Delta_i^-(\Delta_i^+ + \Delta_i^-)]$. Equation (4.1a) was discretized in flux-conserving form in order to ensure numerical mass conservation. At each grid point i only the outward flux $q_{i+1/2}$ was computed, while for the inward flux $q_{i-1/2}$ we reused the outward flux of its left neighbor $i-1$.

The scheme is backward in time and uses an adaptive time step based on a step-doubling algorithm (Press *et al.* 1992) to minimize the computational time. At each step, two solutions are computed, the first (S_B) by using the full time step Δt , the second (S_S) by taking two steps of length $\Delta t/2$. If the error $|S_B - S_S|$, averaged over all grid points, is larger than a specified tolerance (typically 10^{-4}), the step is rejected and repeated after halving the time step. Otherwise, the step is accepted and an extrapolated value $S = 2S_B - S_S$ of the solution is computed which achieves $O(\Delta t^2)$ accuracy. The next time step is then increased by a factor inversely proportional to the error.

The solution at any step was found by solving (4.1) implicitly. The Jacobian of the functions F and G in (4.1) was computed analytically, resulting in a heptadiagonal matrix (three non-zero diagonals on each side of the main diagonal) that was inverted using the standard Gaussian elimination method for banded matrices. A Newton iteration procedure correctly showed quadratic convergence and after a maximum of four Newton iterations the residual never exceeded 10^{-14} .

As the four boundary conditions for the fourth order differential equation (3.14) we chose no-flux and zero slope at both ends ($\xi = \pm 1$). These conditions must be expressed in the hyperbolic system. Thus, it is necessary to know how slopes and fluxes given in Cartesian coordinates transform to hyperbolic ones. For slopes, we have

$$\frac{dy_s}{dx} = \frac{h(\epsilon^2 h h' + \xi - r)}{2r(r - \xi)} \approx \epsilon \left(h' - \frac{h}{2\xi} \right), \quad (4.2a)$$

$$\frac{dx_s}{dy} = -\frac{\epsilon h}{2r} - \frac{\epsilon^3 h^2 h'}{2r(r + \xi)} \approx -\epsilon \left(h' - \frac{h}{2\xi} \right), \quad (4.2b)$$

where (4.2a) is used if the free surface is written as $y_s(x)$ (numerically more accurate for $y > x$, i.e. at $\xi = -1$), while (4.2b) is used if the surface is written as $x_s(y)$ (for $\xi = 1$). Since $\epsilon h \ll |\xi|$ is always true at the boundaries, we can use the Taylor-approximated relations in (4.2). A similar reasoning applies for the flux boundary condition. The flux in (x, y) is the volume of fluid crossing a line $x = \text{constant}$ (for $x > y$) or $y = \text{constant}$ (for $y > x$) in unit time. The flux in (ξ, η) , on the other hand, is the volume of fluid crossing a line $\xi = \text{constant}$ in unit time. While it is cumbersome to transform a flow rate given in (x, y) into its (ξ, η) -equivalent, we note that in the lubrication limit the two flow rate definitions coincide to within a term of $O(\epsilon^2)$ when $\epsilon h \ll |\xi|$. This is certainly

the case at the boundaries, since far away from the corner the lines of constant ξ tend to coincide with the lines of constant x (for $x > y$) or constant y (for $y > x$). Thus, the flux specified in the (x, y) system can be directly applied in the (ξ, η) system. Further details of the numerical scheme, along with results from convergence tests, are given in appendix B.

5. Results

In this section we present results from the numerical integration, before comparing our model to experimental data in the next section. We begin by considering the evolution of an initially L-shaped thin film under surface tension alone ($Bo = 0$). This is shown in figure 4 for $\epsilon = 0.04$. For this initial condition, the expansion parameter ϵ can be related to the filling fraction F_R of the unit Cartesian box by $F_R = \epsilon(1 - \ln \epsilon)$. The two can thus be used interchangeably as a measure of the film thickness. For $\epsilon = 0.04$, $F_R = 0.169$. The sharp corner in the initial profile is immediately smoothed out by surface tension ($t = 3.6 \cdot 10^{-4}$), which then progressively reduces the gradient of curvature everywhere. Eventually, the fluid assumes the shape of a quarter of a circle ($t = 10^5$), whose radius of curvature is determined only by the filling fraction. We checked that different initial conditions (e.g. a hyperbola) with the same filling fraction led to the same steady state. Note that this is exactly what we expect. We do not claim that this is the only way to approach this problem, but rather we use it as a test case for the method.

The steady state for several values of F_R is shown in figure 5(a). For $F_R < F_{Rcr} = 1 - \pi/4 \simeq 0.215$, the liquid retracts towards the corners, where it forms a quarter of a circle. For $F_R > F_{Rcr}$, there is enough fluid for the curvature to be the same everywhere. In all cases, the curvature gradient is everywhere zero (except in the small transition region between the two regions of constant curvature) and the curvature of the circular region (figure 5b) matches the one computed theoretically, since the steady state is the state that minimizes the surface area (here, the perimeter), given F_R . Note that the model performs accurately even for rather large values of ϵ , the largest filling fraction in figure 5 corresponding to $\epsilon = 0.3$.

The time scale required to reach steady state as a function of the filling fraction can be inferred from figure 6. Here, the distance from the origin of the free surface point lying on $x = y$ (that is, $\xi = 0$) — normalized by its steady-state value — is plotted versus time. Evolution is faster for larger filling fractions. The film reaches steady state after approximately $t = 0.1$ for $F_R = 0.662$ and takes 10^6 times longer for $F_R = 0.008$. Thus, for small filling fractions the evolution is very slow. This reflects the fact that the viscous drag exerted by the boundaries plays a more important role when the film is thin.

The typical velocity profile across a thin film in lubrication theory over a solid unidirectional substrate is parabolic (e.g. Myers 2003). In §3.3 we showed that — if the position-dependent terms in the governing equations are also expanded in ϵ — the resulting velocity profile (3.18) is parabolic in η (but singular at $\xi = 0$). On the other hand, the full velocity profile (3.11) is not parabolic, and we expect the difference to be more pronounced nearest to the corner. Figure 7 compares the shape of u_0 to its parabolic approximation (3.18), each normalized by its maximum value, as we are only interested in the shape of the profile. The normalized profiles depend on ϵ and ξ only through the ratio $\epsilon/|\xi|$. Figure 7(a) compares the two velocity profiles for $\epsilon/|\xi| = 10^5$, while figure 7(b) shows the maximum deviation of u_0 from a parabola as a function of $\epsilon/|\xi|$. For each value of $\epsilon/|\xi|$, the deviation at each η was computed as the relative difference between the two normalized velocities defined in figure 7(a). Away from the corner (large $|\xi|$) and for very thin films (small ϵ), the velocity profile is indistinguishable from parabolic.

However, even very close to the corner (small $|\xi|$) and for relatively thick films (large ϵ), the relative deviation of u_0 from parabolic never exceeds 3.5%. For example, for $\epsilon = 0.01$, the velocity profile is everywhere parabolic to within 1%, except for the region $|\xi| < 0.01$ closest to the corner.

When $Bo \neq 0$, the evolution is governed by the competition between gravity and surface tension. Figure 8 shows two cases — $Bo = 4$ and $Bo = 200$ — for $F_R = 0.169$. Gravity destroys the symmetry about $\xi = 0$, the film drains down from the vertical wall and forms a pool along the bottom. This behaviour is accentuated for larger Bo . Figure 9 shows the steady state shape for several values of Bo . The fact that some fluid is retained on the vertical wall by surface tension even at steady state is due to the symmetry boundary condition applied at $\xi = -1$. As Bo increases, more fluid drains from the vertical wall and the pool at the bottom becomes larger. It is straightforward to show that for this steady case, (3.14) simplifies to the Young-Laplace equation for a static meniscus (e.g. Landau & Lifschitz 1987).

If the direction of gravity is reversed, a liquid film coating a ceiling near a vertical wall can be modelled. Gravity drives the fluid away from the ceiling, either by drainage along the vertical wall or by dripping. Lateral drainage prevails when F_R is large and Bo is small. For small F_R and large Bo , the liquid becomes unstable and forms pendant drops before it has the time to drain down the wall, as shown in figure 10. Up to five drops were observed, the number of drops increasing with Bo . Yiantsios & Higgins (1989) investigated the formation of drops from a thin viscous film, showing that for small Bo steady-state pendant drops are possible and correctly predicted by lubrication theory. Using their notation, all six steady-state cases in figure 10 qualify as small Bo cases. Furthermore, their theory predicts the drop's length to increase with F_R and to decrease with Bo : figure 10 shows that both tendencies are successfully captured by our model. Larger Bo cannot be achieved as the numerical film ruptures. This is also in line with Yiantsios and Higgins' conclusion that lubrication theory fails at large Bond numbers, when the interface becomes highly convoluted. The decay in amplitude of the drops towards the corner is due to the asymmetry introduced by the presence of the vertical wall. We did not concern ourselves extensively with pendant drops, since our change of coordinates is certainly not the simplest approach to this case. However, the fact that our model is able to capture steady-state pendant drops correctly gives further confidence in its validity.

6. Comparison with experiments

As a validation of the model, a comparison with a set of simple experiments was carried out. The aim of these experiments is by no means to investigate new physics, but only to assess the performance and the limitations of the model. Some more physically relevant applications for future investigations are suggested in the Discussion section.

The experiments concern the evolution of a thin layer of fluid under the combined action of surface tension and gravity. The experimental device, shown in figure 11, consists of a square Plexiglas box without a lid, with a Teflon coated bottom to maximize the contact angle with the fluid and to minimize pinning of the contact line. The inner size of the box is $5 \times 5 \text{ cm}^2$. A smaller, 'cookie-cutter'-like shape, $4.4 \times 4.4 \text{ cm}^2$, was positioned inside the box, so that the two were concentric and their four sides parallel, forming a 0.3 cm wide gap between the inner sides of the box and the shape. The corners of the shape were smooth, with a radius of curvature of 0.3 cm. The gap was filled with a glycerol-water solution, dyed with thymol blue for visualization purposes, whose typical

depth was less than 1 mm. The ‘cookie-cutter’ was removed suddenly by pulling it up vertically.

Digital pictures of the steady state were taken at a resolution of 6 Megapixels. Digital processing was used to reconstruct the position of the interface. After converting the image to a gray-scale color map, the interface was defined by setting a threshold value of gray. The reconstructed interface is insensitive to small changes in this threshold value. Only experiments in which symmetry among the four corners was preserved were retained, to obtain an easy comparison of the steady state with that obtained from the model, in which a zero-slope and a zero-flux boundary conditions at both ends were imposed. F_R for the model was determined by integrating the area of the reconstructed profile. One example of comparison is shown in figure 12 for $Bo = 0$ and $F_R = 0.19$. The agreement is striking.

One discrepancy between the model and the experiments derives from the fact that the experiment did not evolve up to the theoretical steady state (e.g. figure 5). In particular, the thickness of the film at $\xi = \pm 1$ did not tend to zero. This discrepancy is due to three-dimensional effects. Since the profile has a finite depth and a non-trivial shape in the third dimension, an additional curvature exists. The latter is opposite in sign to the main curvature and becomes important as the film approaches steady state. Ultimately, when the depth of the film becomes comparable to its width, the evolution is arrested. In addition, pinning effects cannot completely be avoided, despite the fact that a very hydrophobic substance (Teflon) was chosen to coat the bottom of the box. This contributes to the premature arrest of the evolution. Note that viscosity is irrelevant in determining the steady-state shape — determined only by F_R and Bo — but influences the time scale of the evolution. To obtain a comparison with the experiments, the numerical model was integrated up to steady state and the profile at some time t that most closely matched the experimental observation was chosen. The best match was determined by minimizing the absolute value of the difference of h from the model and from the experiments. We are thus assuming that the evolution in the experiments followed the predictions up to a certain time, then stopped due to three-dimensional effects. This points both to the limitation and the accuracy of the model. The limitation is clear in that any three-dimensional effects cannot be captured in the current analysis (see the Discussion section for more details). On the other hand, the comparison in figure 12 shows that the model is extremely accurate, in that it almost perfectly captures the shape of the steady-state profile, up to the point where three-dimensional effects become dominant and arrest the evolution.

Figure 13 reinforces this conclusion, showing that the agreement is indeed excellent irrespective of the filling fraction. Unfortunately, no consistent pattern was observed in the times of best fit, nor could they be reliably linked to the adjustment process in the experiment. The experiments could be enhanced by eliminating the ‘pinning’ effects, which would result in a better comparison with the predicted steady state. However, these limitations are due to the experimental setup and since the focus of this paper is on the model, we did not proceed further in the experimental investigation.

The effects of gravity were introduced by slightly tilting the experimental device. In this case, no ‘cookie-cutter’ was used. Instead, a quantity of fluid was injected along the four walls of the box, so as to wet all of them. Most of the fluid was injected adjacent to one of the four sidewalls while the box was held with its bottom horizontal. Viscosity prevented it from flowing under this configuration. The box was then tilted suddenly by a small angle (2.3°) so that the fluid started to flow down towards the opposite wall evolving under gravity and surface tension, and eventually reached steady state. The image processing and the method of comparison with the model were the same as in the

previous case. Figure 14 shows results for $Bo = 15$ and four values of F_R . The agreement is again very good and demonstrates the ability of the model to capture the effects of gravity. A small discrepancy is observed at $\xi = -1$, where for simplicity we continued to use the boundary condition $dx_s/dy = 0$, despite the fact that the film is not necessarily symmetric in these experiment.

7. Discussion

In the previous sections we have derived an evolution equation for the flow of a thin film in a corner region and applied it to simple test cases. It is now appropriate to discuss the flow configuration in more detail, as well as the advantages and the limitations of this method, in conjunction with its possible use for more practical applications. We emphasize again that the experiments were deliberately kept simple, since their only scope was to serve as a test case for the model. While the focus of this paper has been the development of a new method to apply lubrication theory in a corner, it is hoped that this approach will be helpful in many practical situations where thin films have to negotiate a corner.

Moffatt (1964) described the asymptotic flow of a viscous fluid near a corner of arbitrary angle θ . He found that an infinite geometric progression of eddies can develop, whose size and intensity fall off rapidly due to viscosity. When the sides of the corner are two solid walls, as in the case treated here, eddies can form for $\theta < 146^\circ$. In our configuration, Moffatt's semi-infinite fluid domain is replaced by a thin layer having a free surface, prompting the question of whether eddies can still arise. While our lowest-order model is intrinsically unable to capture eddies (as the lowest-order velocity is approximately parabolic), it is most accurate the thinner the film, where eddies are least likely to develop. Thus, if Moffatt eddies are to form — a question best answered by solving for the full Stokes flow — we would expect them in thicker films, where our approximation loses validity. It is interesting to note that eddies cannot form in a square corner when at least one of the two sides is not a solid wall (Moffatt 1964).

The advantage of our approach over a full numerical solution of the original governing equations is apparent in terms of the computational time — each of the simulations presented in this paper took only a few seconds on a 1.8GHz Pentium 4. Furthermore, aside from the complexities of any numerical code dealing with a free surface, this geometry presents additional difficulties in defining a two-dimensional grid, since — as the film becomes thinner — the cells become more and more elongated, eventually making a fully numerical scheme unstable. A clever choice of the grid in a finite element method would be one derived from our change of coordinates (see figure 2). Of course, this choice is not feasible when using finite differences, unless the equations are solved in the (ξ, η) coordinate system. With respect to more general lubrication approaches developed for thin films over topography (e.g. Roy *et al.* 2002), ours has the advantage of being simple both in the formulation and in the implementation. In addition, our method is specifically tailored to a sharp corner, where the curvature and its gradient become singular. This singularity is reflected in the care one must take close to $\xi = 0$, but does not prevent exact integration of the mass conservation equation.

It is interesting to compare the present approach with the method of spines, originally developed by Kistler & Scriven (1983) (see also Heil & White 2002). In that method the film thickness is measured in the direction of certain pre-determined vectors — the spines — originating from the substrate. Conditions are imposed on the choice of the spines such that they do not intersect inside the fluid domain. Conceptually, this has some similarity with our approach, as we measure the thickness of the film along η . Lines

of constant ξ could then be interpreted as curved spines, while the orthogonality of the coordinate system guarantees that our ‘spines’ do not intersect. With respect to ours, the method of spines has the advantage of being applicable to more general substrates. On the other hand, Heil & White (2002) showed that for highly curved substrates lubrication theory does not ensure conservation of volume. They therefore developed a modified lubrication equation — to be used with the method of spines — by introducing an appropriately chosen film density. However, they recognize that this *ad hoc* modification is not ‘rational’ in the sense of a long-wavelength asymptotic theory. In this respect, our change of coordinates has the merit of implicitly ensuring volume conservation, as well as being a more direct application of the traditional lubrication approach, based solely on the recognition that the film is everywhere thin if measured along η .[†]

While the experiments demonstrated that the model correctly reproduces the evolution of a thin film in a corner under surface tension and gravity, they also pointed out the importance of three-dimensional effects. The applicability of our two-dimensional model therefore needs to be carefully assessed on a case-by-case basis. As a possible extension, one could apply the present analysis to a corner flow in a Hele-Shaw cell, where two plates bound the fluid in the third dimension. It would then be necessary to integrate the governing equations over the thickness of the Hele-Shaw cell before proceeding with lubrication theory. This would introduce additional terms, in particular the contribution from the second curvature.

The use of a reduced model coupled with a change of coordinates can be exploited also to investigate the dynamics of foams, mentioned in the Introduction. While several factors such as evaporation could affect the evolution of a foam, one approach to modelling a two-dimensional foam is to idealize it as a periodic array of air bubbles immersed in a liquid matrix (Pozrikidis 2002). When the bubbles expand, for example due to a drop in ambient pressure, liquid drains into corner-like regions known as Plateau borders, eventually leading to the breakup of the thin films separating adjacent bubbles. Pozrikidis (2002) used arrays of both hexagonal and square cells, finding little qualitative difference between the two. Hexagonal cells are more appropriate, as foams make angles of $2\pi/3$. A corner of $\pi/2$ (Stocker & Hosoi 2004) can be considered a simplified prototype that captures the dominant effects of the abrupt change in direction. Alternatively, one could pursue the change of coordinates $(\xi, \eta) = (Re, Im) [(x + iy)^{3/2}]$, for an angle of $2\pi/3$: the resulting evolution equation would be modified, but the method remains unchanged. One could then obtain solutions for the shape of the interface at very long times — unlike existing numerical models (Pozrikidis 2002) — and eventually determine when the liquid filaments break. The main advantage of this approach is that a single solution for the entire flow domain would be obtained, bypassing the decomposition into several regions and their matching adopted by several authors (e.g. Breward & Howell 2002). We should note that an alternative, very elegant small-slope approximation is that of Schwartz & Roy (2003), who avoid the corner altogether by exploiting the symmetries in the flow configuration. A comparison between our method and theirs would be interesting, and would allow one to verify the accuracy of their (implicit) assumption that the $\pi/6$ angle formed by the free surface at the foam’s axis of symmetry can be considered small. Lastly, one could conceive adding an equation for the surfactant distribution to the model, as surfactants strongly influence the shape and lifetime of foams (e.g. Breward & Howell 2002; Schwartz & Roy 2003).

[†] Recently Jensen, Chini and King (J. Engng. Math., accepted) applied the method of spines to a lubrication model of an interior corner, again using a film density to ensure volume conservation.

The application of our model to ‘fishbone’ instability of Spiegelberg & McKinley (1996) would require three main modifications. First, the non-Newtonian stress tensor could make the analytical integration of mass conservation more difficult. In general, we expect additional evolution equations associated with the fluid’s constitutive relation (e.g. Schultz 1987; Olagunju 1999). Second, the asymmetric stretching of the domain must be taken into account (e.g. only along y , not along x). Third, ‘mixed’ boundary conditions must be used — no-slip on the bottom plate and symmetry across the centerline of the vertical filament. A linear stability analysis would then have to be performed numerically to capture the ‘fishbone’ instability. We did not perform a stability analysis on our solution as Spiegelberg and McKinley’s experiments exhibit no instability when Newtonian fluids are used.

8. Conclusions

We have shown that lubrication theory can be used in an interior corner following an appropriate change of coordinates. The equations of motion were written in a hyperbolic coordinate system and the assumption that the liquid film is everywhere thin led to a single evolution equation for its thickness. The full curvature and gravity terms were retained. The simple η –dependence of the lowest order velocity field allowed us to integrate the full equation of mass conservation exactly (to within one integral), with the great advantage of ensuring conservation of mass. We showed that care must be taken when ξ becomes small, due to the presence of position-dependent terms that, if approximated, make the equations singular at $\xi = 0$. However, even when such an approximation is made, we showed that the effects on the profile evolution and steady state are negligible for small film thicknesses. The numerical integration of the evolution equation has been described and implemented. The outcomes were successfully compared to theoretical results and simplified laboratory experiments of the evolution of a thin film in a corner under surface tension and gravity.

We would like to thank Darren Crowdy, David Vener, Constantin Pozrikidis and José Bico for discussions during the early stage of this manuscript. This research was partially supported by 3M and by NSF grant 0243591.

Appendix A. Details of the hyperbolic coordinates

This appendix provides more details on the derivations in § 2 and § 3.

A.1. Change of coordinates

The following (dimensional) expressions were used in the change of coordinates $\xi = x^2 - y^2$, $\eta = 2xy$. All notation is defined in the text.

$$y = \left(\frac{r - \xi}{2} \right)^{1/2}, \quad x = \left(\frac{r + \xi}{2} \right)^{1/2}, \quad (\text{A } 1a,b)$$

$$\frac{\partial x}{\partial \eta} = -\frac{\partial y}{\partial \xi} = \frac{y}{2r}, \quad \frac{\partial x}{\partial \xi} = \frac{\partial y}{\partial \eta} = \frac{x}{2r}, \quad (\text{A } 1c,d)$$

$$\frac{\partial r}{\partial \xi} = \frac{\xi}{r}, \quad \frac{\partial r}{\partial \eta} = \frac{\eta}{r}, \quad (\text{A } 1e,f)$$

$$\frac{\partial s}{\partial \xi} = -\frac{\xi}{4r^{5/2}}, \quad \frac{\partial s}{\partial \eta} = -\frac{\eta}{4r^{5/2}}, \quad (\text{A } 1g,h)$$

$$f_1 = \frac{1}{s} \frac{\partial s}{\partial \xi} = -\frac{\xi}{2r^2}, \quad f_2 = \frac{1}{s} \frac{\partial s}{\partial \eta} = -\frac{\eta}{2r^2}. \quad (\text{A } 1i,j)$$

The expressions for gradient, divergence, and Laplacian in the hyperbolic coordinates, for example applied to the pressure field p and the velocity field $\mathbf{u} = u\hat{\xi} + v\hat{\eta}$ are (e.g. Arfken 1970):

$$\nabla p = \frac{1}{s} \frac{\partial p}{\partial \xi} \hat{\xi} + \frac{1}{s} \frac{\partial p}{\partial \eta} \hat{\eta}, \quad (\text{A } 2a)$$

$$\nabla \cdot \mathbf{u} = \frac{1}{s^2} \left[\frac{\partial(us)}{\partial \xi} + \frac{\partial(vs)}{\partial \eta} \right], \quad (\text{A } 2b)$$

$$\nabla^2 \mathbf{u} = \nabla \cdot \nabla \mathbf{u} = \frac{1}{s^2} \left[\frac{\partial}{\partial \xi} \left(\frac{\partial \mathbf{u}}{\partial \xi} \right) + \frac{\partial}{\partial \eta} \left(\frac{\partial \mathbf{u}}{\partial \eta} \right) \right], \quad (\text{A } 2c)$$

where $\hat{\xi}$ and $\hat{\eta}$ are the unit vectors along the hyperbolic coordinate axes, given by

$$\hat{\xi} = \frac{((r + \xi)^{1/2}, -(r - \xi)^{1/2})}{\sqrt{2r}} = \left(\frac{x}{\sqrt{r}}, -\frac{y}{\sqrt{r}} \right), \quad (\text{A } 3a)$$

$$\hat{\eta} = \frac{((r - \xi)^{1/2}, (r + \xi)^{1/2})}{\sqrt{2r}} = \left(\frac{y}{\sqrt{r}}, \frac{x}{\sqrt{r}} \right), \quad (\text{A } 3b)$$

The full expression for the Laplacian is derived in appendix A.2. The unit vector $\hat{\mathbf{k}}$ appearing in the gravity term in (2.1a) transforms as

$$\hat{\mathbf{k}} = \frac{1}{s} \frac{\partial y}{\partial \xi} \hat{\xi} + \frac{1}{s} \frac{\partial y}{\partial \eta} \hat{\eta}. \quad (\text{A } 4)$$

If the free surface is denoted by $\eta = h(\xi)$, its position is described by $\mathcal{F}(\xi, \eta) = \eta - h(\xi) = 0$. The unit normal vector $\hat{\mathbf{n}}$ is parallel to the gradient and can thus be computed using (A 2a) as

$$\hat{\mathbf{n}} = \frac{\nabla \mathcal{F}}{|\nabla \mathcal{F}|} = \frac{1}{|\nabla \mathcal{F}|} \left(\frac{1}{s} \frac{\partial \mathcal{F}}{\partial \xi} \hat{\xi} + \frac{1}{s} \frac{\partial \mathcal{F}}{\partial \eta} \hat{\eta} \right) = \frac{-h' \hat{\xi} + \hat{\eta}}{(1 + h'^2)^{1/2}}, \quad (\text{A } 5)$$

where primes denote differentiation with respect to ξ . The unit tangent vector is then

$$\hat{\mathbf{t}} = \frac{\hat{\xi} + h' \hat{\eta}}{(1 + h'^2)^{1/2}}. \quad (\text{A } 6)$$

Using (A 2a) the stress tensor $\mathbf{\Pi}$ in (2.3) becomes:

$$\mathbf{\Pi} = \begin{pmatrix} -p + \frac{2\mu}{s} \left(\frac{\partial u}{\partial \xi} - \frac{\eta v}{2r^2} \right) & \frac{\mu}{s} \left(\frac{\partial v}{\partial \xi} + \frac{\partial u}{\partial \eta} + \frac{\eta u + \xi v}{2r^2} \right) \\ \frac{\mu}{s} \left(\frac{\partial v}{\partial \xi} + \frac{\partial u}{\partial \eta} + \frac{\eta u + \xi v}{2r^2} \right) & -p + \frac{2\mu}{s} \left(\frac{\partial v}{\partial \eta} - \frac{\xi u}{2r^2} \right) \end{pmatrix}. \quad (\text{A } 7)$$

A.2. Laplacian

The Laplacian of $\mathbf{u} = u\hat{\xi} + v\hat{\eta}$ appearing in the viscous terms of the momentum equations is somewhat lengthy to compute because the unit vectors $\hat{\xi}$ and $\hat{\eta}$ (A 3) are position-dependent, resulting in

$$\nabla^2 \mathbf{u} = \frac{1}{s^2} \left[\frac{\partial^2 u}{\partial \xi^2} \hat{\xi} + \frac{\partial^2 v}{\partial \xi^2} \hat{\eta} + 2 \frac{\partial u}{\partial \xi} \frac{\partial \hat{\xi}}{\partial \xi} + 2 \frac{\partial v}{\partial \xi} \frac{\partial \hat{\eta}}{\partial \xi} + u \frac{\partial^2 \hat{\xi}}{\partial \xi^2} + v \frac{\partial^2 \hat{\eta}}{\partial \xi^2} + \frac{\partial^2 u}{\partial \eta^2} \hat{\xi} + \frac{\partial^2 v}{\partial \eta^2} \hat{\eta} + 2 \frac{\partial u}{\partial \eta} \frac{\partial \hat{\xi}}{\partial \eta} + 2 \frac{\partial v}{\partial \eta} \frac{\partial \hat{\eta}}{\partial \eta} + u \frac{\partial^2 \hat{\xi}}{\partial \eta^2} + v \frac{\partial^2 \hat{\eta}}{\partial \eta^2} \right]. \quad (\text{A } 8)$$

The first derivatives of the unit vectors are

$$\frac{\partial \hat{\xi}}{\partial \xi} = \frac{\eta}{2r^2} \hat{\eta}, \quad \frac{\partial \hat{\eta}}{\partial \xi} = -\frac{\eta}{2r^2} \hat{\xi}, \quad \frac{\partial \hat{\xi}}{\partial \eta} = -\frac{\xi}{2r^2} \hat{\eta}, \quad \frac{\partial \hat{\eta}}{\partial \eta} = \frac{\xi}{2r^2} \hat{\xi}. \quad (\text{A } 9a-d)$$

Since the second derivatives do not naturally split up into a $\hat{\xi}$ and an $\hat{\eta}$ component, dot products with $\hat{\xi}$ and $\hat{\eta}$ must be taken. This yields:

$$\frac{\partial^2 \hat{\xi}}{\partial \xi^2} = -\frac{\eta^2}{4r^4} \hat{\xi} - \frac{\eta \xi}{r^4} \hat{\eta}, \quad \frac{\partial^2 \hat{\eta}}{\partial \xi^2} = -\frac{\eta^2}{4r^4} \hat{\eta} + \frac{\eta \xi}{r^4} \hat{\xi}, \quad (\text{A } 10a,b)$$

$$\frac{\partial^2 \hat{\xi}}{\partial \eta^2} = -\frac{\xi^2}{4r^4} \hat{\xi} + \frac{\eta \xi}{r^4} \hat{\eta}, \quad \frac{\partial^2 \hat{\eta}}{\partial \eta^2} = -\frac{\xi^2}{4r^4} \hat{\eta} - \frac{\eta \xi}{r^4} \hat{\xi}, \quad (\text{A } 10c,d)$$

where we have used

$$\frac{\partial}{\partial \xi} \left(\frac{1}{r^{1/2}} \right) = -\frac{\xi}{2r^{5/2}}, \quad \frac{\partial}{\partial \eta} \left(\frac{1}{r^{1/2}} \right) = -\frac{\eta}{2r^{5/2}}, \quad (\text{A } 11a,b)$$

$$\frac{\partial}{\partial \xi} \left(\frac{1}{r^{5/2}} \right) = -\frac{5\xi}{2r^{9/2}}, \quad \frac{\partial}{\partial \eta} \left(\frac{1}{r^{5/2}} \right) = -\frac{5\eta}{2r^{9/2}}. \quad (\text{A } 11c,d)$$

We can now rewrite (A 8) by separating the terms contributing to the ξ -momentum equation $((\nabla^2 \mathbf{u}) \cdot \hat{\xi})$ from those contributing to the η -momentum equation $((\nabla^2 \mathbf{u}) \cdot \hat{\eta})$. After some simplifications we find:

$$(\nabla^2 \mathbf{u}) \cdot \hat{\xi} = \frac{1}{s^2} \left[\frac{\partial^2 u}{\partial \xi^2} + \frac{\partial^2 v}{\partial \eta^2} - \frac{1}{r^2} \left(\eta \frac{\partial v}{\partial \xi} - \xi \frac{\partial v}{\partial \eta} + \frac{u}{4} \right) \right], \quad (\text{A } 12a)$$

$$(\nabla^2 \mathbf{u}) \cdot \hat{\eta} = \frac{1}{s^2} \left[\frac{\partial^2 v}{\partial \xi^2} + \frac{\partial^2 u}{\partial \eta^2} - \frac{1}{r^2} \left(-\eta \frac{\partial u}{\partial \xi} + \xi \frac{\partial u}{\partial \eta} + \frac{v}{4} \right) \right]. \quad (\text{A } 12b)$$

Appendix B. Details of the numerical solution

This appendix provides details on the numerical scheme used to integrate the evolution equation (3.14). The grid along ξ is determined as follows. Once the filling fraction F_R and the number of grid points N have been chosen, the first $N/2$ grid points are taken to be $(x_i, y_i) = (\Delta, 1 - (i-1)dy)$, for $i = 1 \dots N/2$, with $\Delta = 1 - \sqrt{1 - F_R}$ and $dy = (1 - \Delta - 2/N)/(N/2 - 1)$. The remaining $N/2$ grid points are found by symmetry about $x = y$. The ξ_i coordinate of the i th grid point is then $\xi_i = x_i^2 - y_i^2$. For this grid,

$-\xi_{max} < \xi < \xi_{max}$, where $\xi_{max} = 1 - \Delta^2$. The grid points are therefore uniformly spaced along the Cartesian axes, so the density of grid points is parabolically increasing with ξ as $\xi \rightarrow 0$. This method avoids $\xi = 0$ being a grid point, a necessary precaution here since the approximate version of the evolution equation is used (see §3.3 for more details). If we take $h_i = 2x_i y_i$ initially, the initial condition corresponds to a film of uniform thickness Δ along both Cartesian axes (an L-shape).

Numerical tests were carried out for $F_R = F_{Rcr} = 0.215$, $Bo = 0$ and $N = 500$. The initial and boundary conditions were the same as in figure 5. The total integration time was $t = 10^5$, enough in all cases to achieve steady state. The effect of varying the number of grid points N can be seen from figure 15, where the error in the steady-state curvature is plotted against N . The steady-state curvature is constant over ξ and equal to one, since $F_R = F_{Rcr}$. However, a small correction is required due to the change of coordinates. At $t = 0$, $-\xi_{max} < \xi < \xi_{max}$ corresponds to the unit Cartesian box. As the film evolves, it becomes thinner at $\xi = \pm \xi_{max}$, thus corresponding to a box slightly smaller than the unit box in Cartesian coordinates. This artificial shrinking of the domain implies that the amount of fluid F_R needs to be accommodated in a smaller-than-unity box. Thus, the expected curvature is slightly larger than the theoretical one, its exact value being dependent on N . While this is admittedly an artifact of the numerical scheme and is described further below, its effect is of $O(\epsilon)$. (One could apply the boundary conditions at a ξ -position that is variable in time, according to the thickness of the film at the boundary, making the grid time-dependent. This would introduce an additional complication that was not pursued in this paper). In particular, it can be seen that the curvature predicted by the model converges towards the expected one as the number of grid points increases. $N = 500$ was considered sufficient for the purposes of this paper.

The fluid volume A (i.e. the area) can be computed as:

$$A = \int_{\xi} \int_0^{\epsilon h(\xi)} s^2 d\eta d\xi = \frac{1}{4} \int_{\xi} \ln \left[\frac{\epsilon h + \sqrt{\xi^2 + \epsilon^2 h^2}}{|\xi|} \right] d\xi. \quad (B 1)$$

The loss of volume over $t = 10^5$ was always less than 0.4%, which can be attributed to the large values attained by R_{approx} (3.20) for small $|\xi|$.

The numerical scheme was implemented in Fortran. Fortran's built-in hypergeometric function routine is too inaccurate for our purposes. Thus we approximated the hypergeometric functions piecewise using polynomials. The logarithm (\log_{10}) of the hypergeometric function's argument was split into 100 intervals, from -6 to +4 in increments of 0.1. In each interval, an n th order polynomial was fitted to the logarithm of the hypergeometric function, with the best-fit coefficients determined using Matlab. We found that $n = 14$ resulted in the best compromise between accuracy and stability. Ultimately, this is equivalent to using a table of numbers for the hypergeometric functions, but has the advantage of obtaining a high accuracy — better than 10^{-10} for all values of the argument of the hypergeometric functions — without storing a huge amount of numbers.

REFERENCES

- ABRAMOWITZ, M. & STEGUN, I. A. 1965 *Handbook of mathematical functions: with formulas, graphs, and mathematical tables*. Dover.
- ARFKEN, G. B. 1970 *Mathematical methods for physicists*. Academic Press.
- BERTOZZI, A. L. & PUGH, M. C. 1998 Long-wave instabilities and saturation in thin film equations. *Comm. Pure Appl. Math.* **51**, 625–661.
- BICO, J. & QUÉRÉ, D. 2002 Rise of liquids and bubbles in angular capillary tubes. *J. Colloid. Interf. Sc.* **247**, 162–166.
- BREWARD, C. J. W. & HOWELL, P. D. 2002 The drainage of a foam lamella. *J. Fluid Mech.* **458**, 379–406.
- EGGERS, J. & DUPONT, T. F. 1994 Drop formation in a one-dimensional approximation of the Navier-Stokes equation. *J. Fluid Mech.* **262**, 205–221.
- GROTBERG, J. B. 1994 Pulmonary flow and transport phenomena. *Ann. Rev. Fluid Mech.* **26**, 529–571.
- HAZEL, A. L. & HEIL, M. 2002 The steady propagation of a semi-infinite bubble into a tube elliptical or rectangular cross-section. *J. Fluid Mech.* **470**, 91–114.
- HEIL, M. & WHITE, J. P. 2002 Airway closure: surface-tension-driven non-axisymmetric instabilities of liquid-lined elastic rings. *J. Fluid Mech.* **462**, 79–109.
- HILGENFELDT, S., KOEHLER, S. A. & STONE, H. A. 2001 Dynamics of coarsening foams: accelerated and self-limited drainage. *Phys. Rev. Letters* **86**, 4704–4707.
- HOSOI, A. E. & MAHADEVAN, L. 1999 Axial instability of a free surface front in a partially-filled rotating cylinder. *Phys. Fluids* **11**, 97.
- HUPPERT, H. E. 1982 The propagation of two-dimensional and axisymmetric viscous gravity currents over a rigid horizontal surface. *J. Fluid Mech.* **121**, 43–58.
- IDA, M. P. & MIKISIS, M. J. 1998*a* The dynamics of thin films I: General theory. *SIAM J. Appl. Math.* **58**, 456–473.
- IDA, M. P. & MIKISIS, M. J. 1998*b* The dynamics of thin films II: Applications. *SIAM J. Appl. Math.* **58**, 474–500.
- KALLIADASIS, S., BIELARZ, C. & HOMSY, G. M. 2000 Steady free-surface thin film flows over topography. *Phys. Fluids* **12**, 1889–1898.
- KISTLER, S. F. & SCRIVEN, L. E. 1983 Coating flows. In *Computational Analysis of Polymer Processing* (ed. J. Pearson & S. Richardson). London: Applied Science Publishers.
- KOLB, W. B. & CERRO, R. L. 1993*a* Film flow in the space between a circular bubble and a square tube. *J. Colloid. Interf. Sc.* **159**, 302–311.
- KOLB, W. B. & CERRO, R. L. 1993*b* The motion of long bubbles in tubes of square cross section. *Phys. Fluids A* **5**, 1549–1557.
- LANDAU, L. D. & LEVICH, B. 1942 Dragging of a liquid by a moving plate. *Acta Physicochimica U.R.S.S.* **17**, 42–54.
- LANDAU, L. D. & LIFSHITZ, E. M. 1987 *Fluid mechanics*. Pergamon.
- MAZOUCHI, A. & HOMSY, G. M. 2001 Free surface stokes flow over topography. *Phys. Fluids* **13**, 2751–2761.
- MOFFATT, H. K. 1964 Viscous and resistive eddies near a sharp corner. *J. Fluid Mech.* **18**, 1–18.
- MORIARTY, J. A. & TERRILL, E. L. 1996 Mathematical modelling of the motion of hard contact lenses. *Euro. J. Appl. Math.* **7**, 575–594.
- MYERS, T. G. 1998 Thin films with high surface tension. *SIAM Rev.* **40**, 441–462.
- MYERS, T. G. 2003 Unsteady laminar flow over a rough surface. *J. Eng. Math.* **46**, 111–126.
- OLAGUNJU, D. O. 1999 A 1-D theory for extensional deformation of a viscoelastic filament under exponential stretching. *J. Non-Newt. Fluid Mech.* **87**, 27–46.
- ORON, A., DAVIS, S. H. & BANKOFF, S. G. 1997 Long-scale evolution of thin liquid films. *Rev. Mod. Phys.* **69**, 931–980.
- POZRIKIDIS, C. 2002 Expansion of a two-dimensional foam. *Eng. Analysis with Boundary Elements* **26**, 495–504.
- PRESS, W. H., TEUKOLSKY, S. A., VETTERLING, W. T. & FLANNERY, B. P. 1992 *Numerical Recipes in Fortran: The Art of Scientific Computing*. Cambridge University Press.
- ROSENZWEIG, J. & JENSEN, O. E. 2002 Capillary-elastic instabilities of liquid-lined lung airways. *J. Biomech. Eng.* **124**, 650–655.

- ROY, R. V., ROBERTS, A. J. & SIMPSON, M. E. 2002 A lubrication model of coating flows over a curved substrate in space. *J. Fluid Mech.* **454**, 235–261.
- RUSCHAK, K. J. 1978 Flow of a falling film into a pool. *AIChEJ* **24**, 705–708.
- SCHULTZ, W. W. 1987 Slender viscoelastic fiber flow. *J. Rheol.* **31**, 733–750.
- SCHWARTZ, L. W. & ROY, R. V. 2003 A mathematical model for an expanding foam. *J. Colloid Interf. Sc.* **264**, 237–249.
- SCHWARTZ, L. W. & WEIDNER, D. E. 1995 Modeling of coating flows on curved surfaces. *J. Eng. Math.* **29**, 91–103.
- SPIEGELBERG, S. H. & MCKINLEY, G. H. 1996 Stress relaxation and elastic decohesion of viscoelastic polymer solutions in extensional flow. *J. Non-Newt. Fluid Mech.* **67**, 49–76.
- STILLWAGON, L. E. & LARSON, R. G. 1988 Fundamentals of topographic substrate leveling. *J. Applied Phys.* **63**, 5251–5258.
- STILLWAGON, L. E. & LARSON, R. G. 1990 Leveling of thin films over uneven substrates during spin coating. *Phys. Fluids A* **2**, 1937–1944.
- STOCKER, R. & HOSOI, A. E. 2004 Corner flow in free liquid films. *J. Engng. Math.* p. accepted.
- THULASIDAS, T. C., ABRAHAM, M. A. & CERRO, R. L. 1995 Bubble-train flow in capillaries of circular and square cross section. *Chem. Eng. Sc.* **50**, 183–199.
- WASAN, D. T., KOCZO, K. & NIKOLOV, A. D. 1994 Mechanisms of aqueous foam stability and antifoaming action with and without oil: a thin film approach. In *Foams: Fundamentals and Applications in Petroleum Industry* (ed. L. L. Schramm), pp. 47–114. American Chemical Society, Washington.
- WEISLOGEL, M. M. 2001 Capillary flow in interior corners: The infinite column. *Phys. Fluids* **13**, 3101–3107.
- WEISLOGEL, M. M. & LICHTER, S. 1998 Capillary flow in an interior corner. *J. Fluid Mech.* **373**, 349–378.
- WONG, H., FATT, I. & RADKE, C. J. 1996 Deposition and thinning of the human tear film. *J. Colloid. Interf. Sci.* **184**, 44–51.
- YIANTSIOS, S. G. & HIGGINS, B. G. 1989 Rayleigh-taylor instability in thin viscous films. *Phys. Fluids A* **1**, 1484–1501.

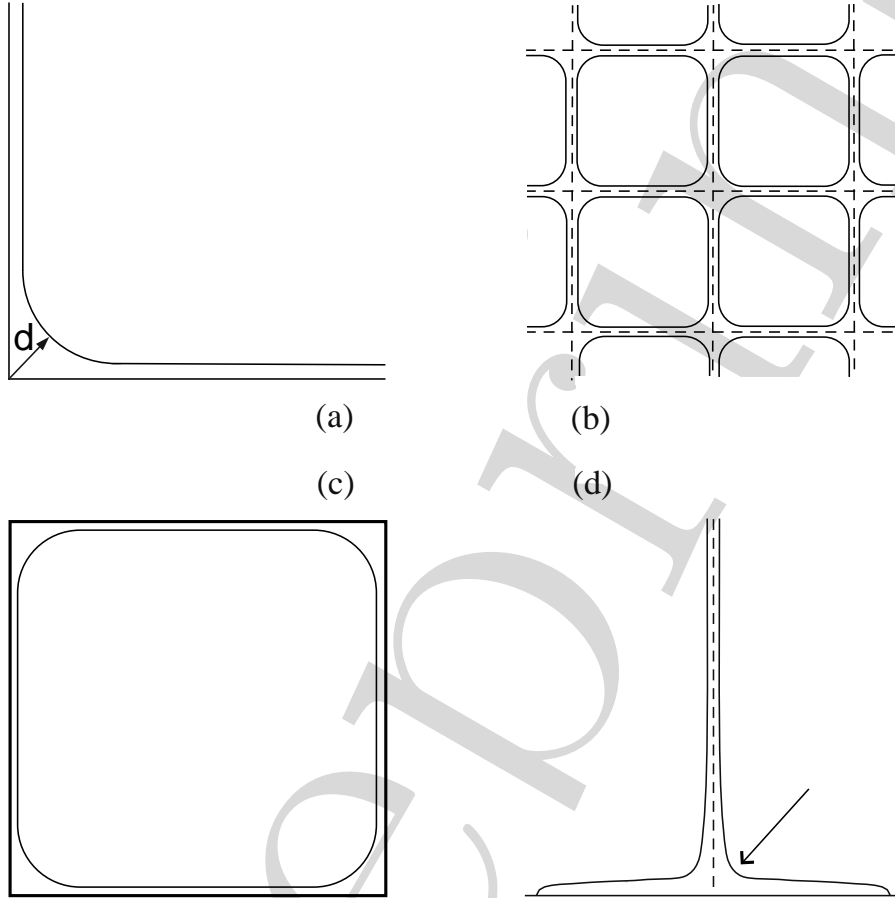


FIGURE 1. (a) Sketch of a thin film in an interior corner. d is the distance from the origin to the point on the profile having $\xi = 0$ (i.e. $x = y$). (b) Coarsening foams are sometimes modelled (e.g. Pozrikidis 2002) as an array of square cells (dashed). The solid lines represent the boundaries between the air bubbles and the liquid phase, the dashed lines are axes of symmetry. (c) Bubble flow in a square capillary, cross-section taken far away from the bubble's ends. The thick line indicates the capillary, the thin line is the surface of the bubble, which is moving out of the page. Such non-axisymmetric bubbles form at small Capillary numbers (< 0.04). (d) Stretching of liquid filaments, as for example in rheological experiments. The arrow indicates the region where 'fishbone' instabilities were observed experimentally by Spiegelberg & McKinley (1996) for non-Newtonian fluids.

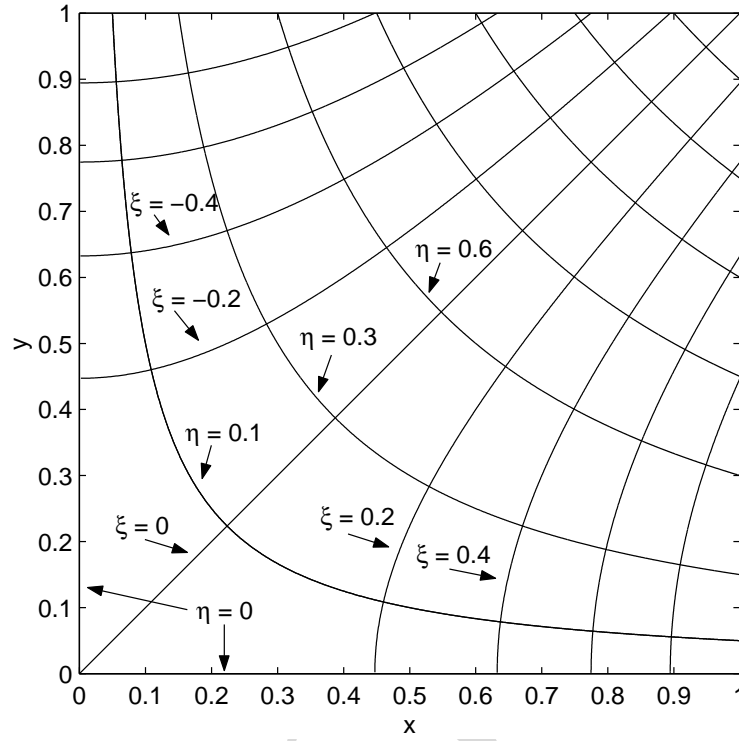


FIGURE 2. The hyperbolic coordinate system ($\xi = x^2 - y^2, \eta = 2xy$).

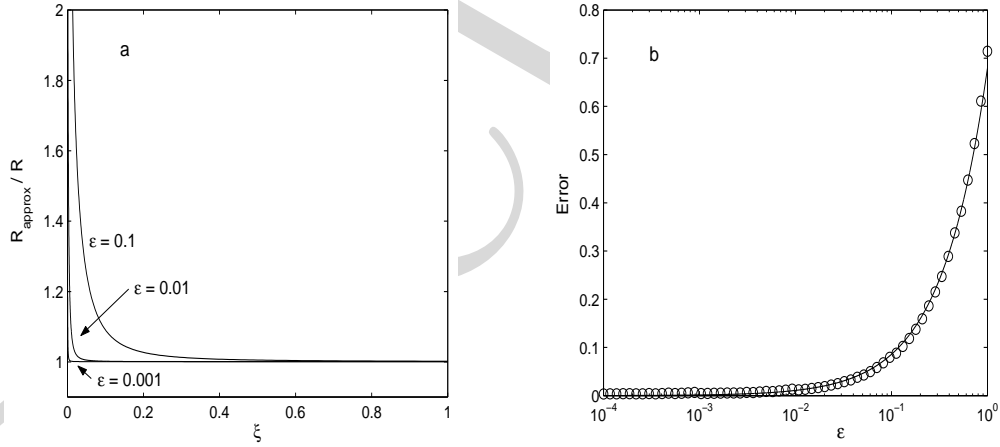


FIGURE 3. (a) Ratio of R_{approx} (3.20) to R (3.15) as a function of the along-wall coordinate ξ , for three values of ϵ . In (3.20) and (3.15) $z = \xi/\epsilon h$. Here $h = 1$ and we used $N = 5000$ grid points. $R_{approx}/R \rightarrow 1$ as $\xi \rightarrow \infty$, indicating that R_{approx} is a good approximation to R unless ξ is very close to zero. (b) The error incurred by approximating R with R_{approx} , computed as the integral of $R_{approx}/R - 1$ over $10^{-5} < \xi \leq 1$, shown as circles. The error grows approximately like $\epsilon^{0.9}$ (the solid line represents $0.67\epsilon^{0.9}$) and vanishes as $\epsilon \rightarrow 0$.

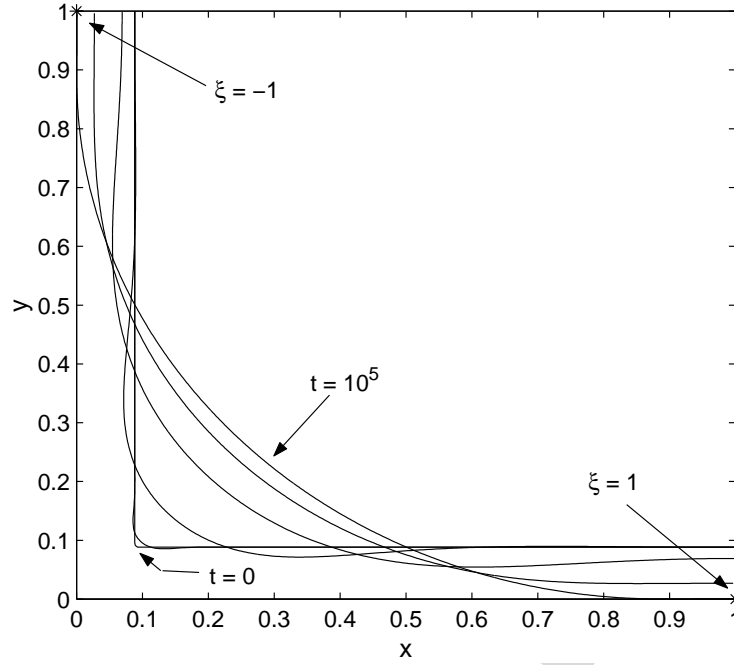


FIGURE 4. Snapshots of the evolution of a thin film governed by surface tension ($Bo = 0$) for $F_R = 0.169$ ($\epsilon = 0.04$). The profiles correspond to the dimensionless times $t = 0, 3.6 \cdot 10^{-4}, 0.67, 22.9, 112.6, 10^5$. The initial condition ($t = 0$) consists of an L-shaped region of liquid with a sharp corner. By $t = 10^5$ the profile has reached steady state. No-flux and zero-slope boundary conditions were imposed at both ends ($\xi = \pm 1$).

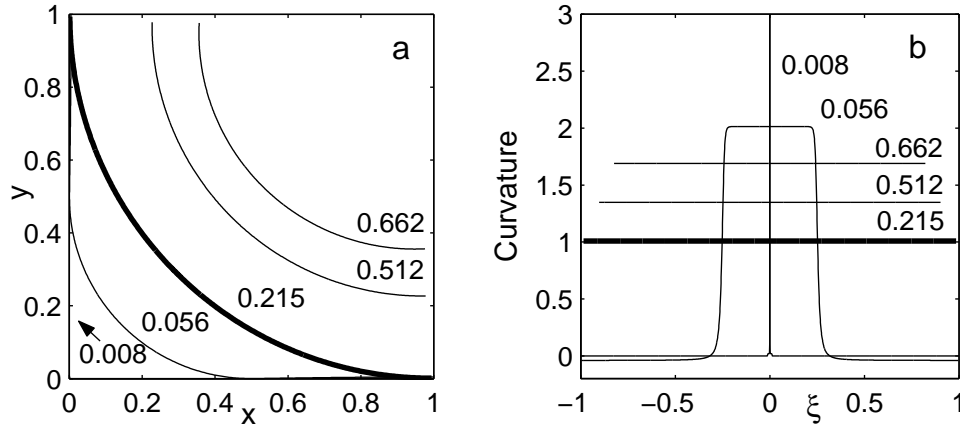


FIGURE 5. Steady-state profile (a) and curvature (b) of a thin film governed by surface tension ($Bo = 0$) for several values of F_R , indicated in the plots. For the critical filling fraction $F_R = 1 - \pi/4 \simeq 0.215$ ($\epsilon = 0.055$) the steady-state configuration is a quarter of a circle with curvature 1 (thicker lines in (a) and (b)). All cases were simulated up to $t = 10^5$ and no further evolution occurred for larger times. The constant value of the curvature indicates the steady-state profiles predicted by the model are correct, as they correspond to the states of minimum energy. The initial and boundary conditions are as in figure 4.

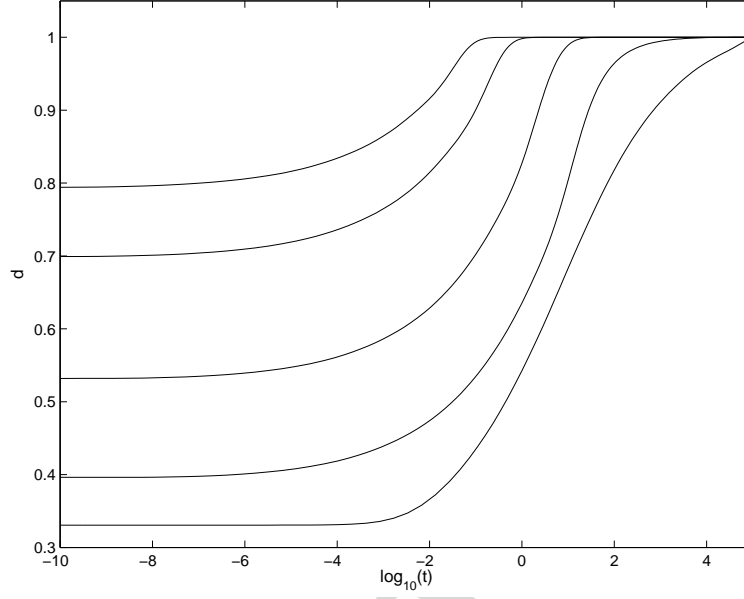


FIGURE 6. The time scale for evolution to steady state for $Bo = 0$ and $F_R = 0.008, 0.215, 0.330, 0.512, 0.662$ (bottom to top). Thinner films take longer to reach steady state due to the larger influence of viscous drag. d is the distance indicated in figure 1 (a), normalized by its steady-state value. The initial and boundary conditions are as in figure 4.

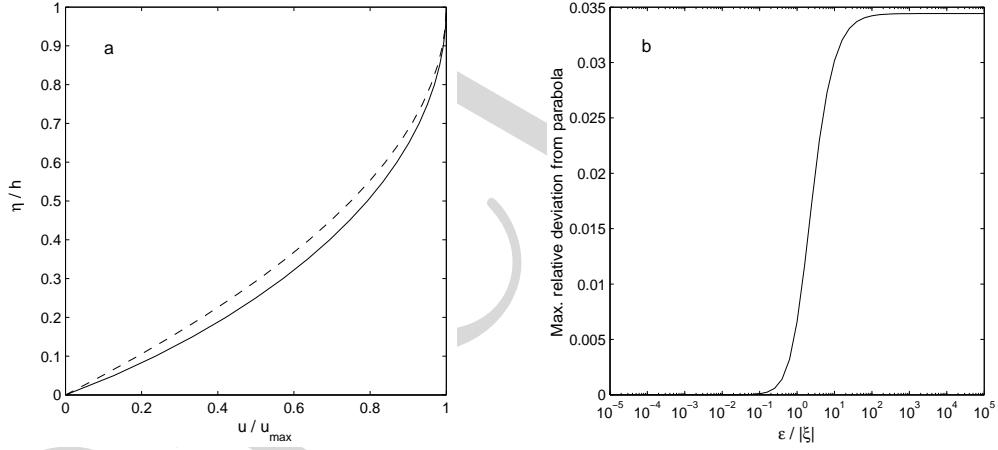


FIGURE 7. (a) The full velocity profile (3.11, solid line) and the approximated velocity profile (3.18, dashed line) for $\epsilon/|\xi| = 10^5$ and $h = 1$. The approximated velocity is exactly parabolic in η . Each velocity has been normalized by its value at $\eta = h$. (b) The maximum relative deviation of the full velocity profile (3.11) from a parabolic one as a function of $\epsilon/|\xi|$.

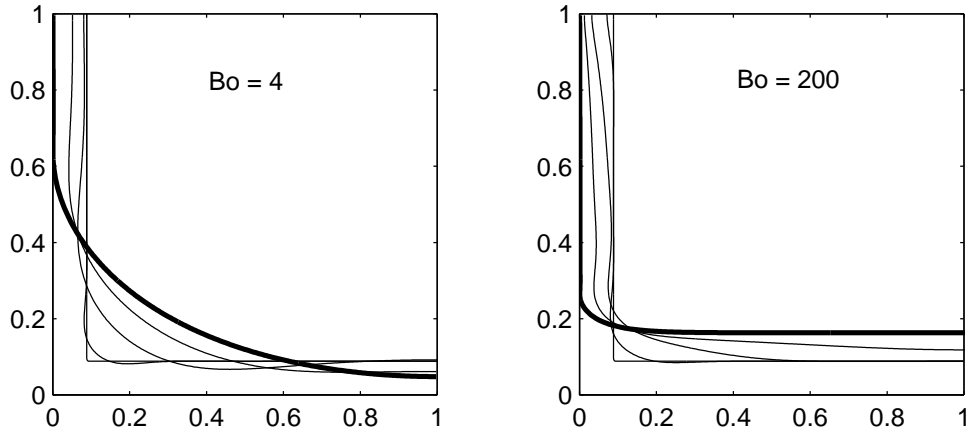


FIGURE 8. The evolution of a thin film governed by gravity and surface tension for two values of Bo and $F_R = 0.169$ ($\epsilon = 0.04$). The profile with a sharp corner corresponds to the initial condition, while the bold line corresponds to the steady state. The profile for $Bo = 4$ is shown at $t = 0, 0.016, 3.1, 23.2, 10^5$, while that for $Bo = 200$ is shown at $t = 0, 0.027, 0.3, 1.9, 10^3$. The initial and boundary conditions are as in figure 4.

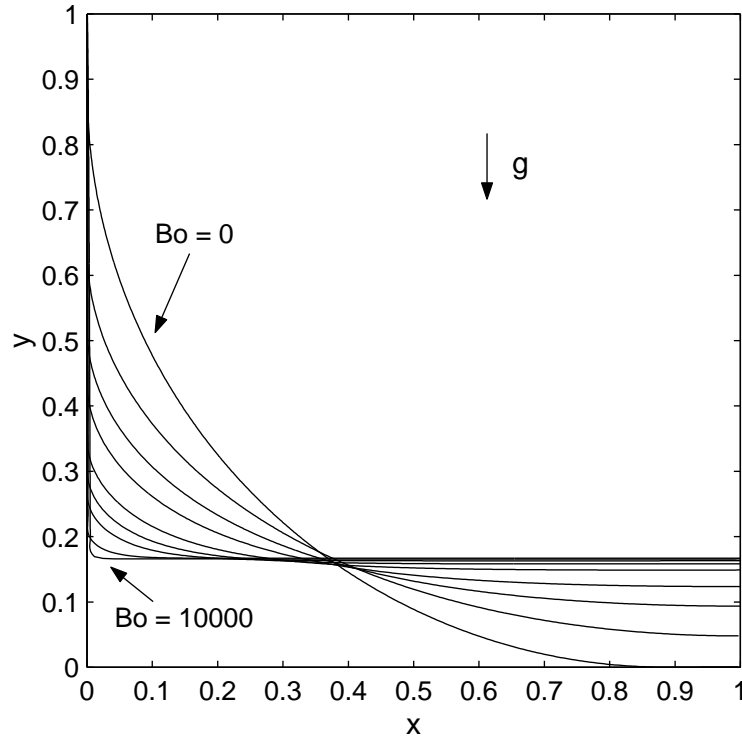


FIGURE 9. The steady state of a draining thin film governed by gravity and surface tension for several values of Bo (0, 4, 10, 20, 50, 100, 200, 1000, 10000) and $F_R = 0.169$ ($\epsilon = 0.04$). Gravity forces the film to drain from the vertical wall and to form a pool at the bottom, whose size increases with Bo . The initial and boundary conditions are as in figure 4.

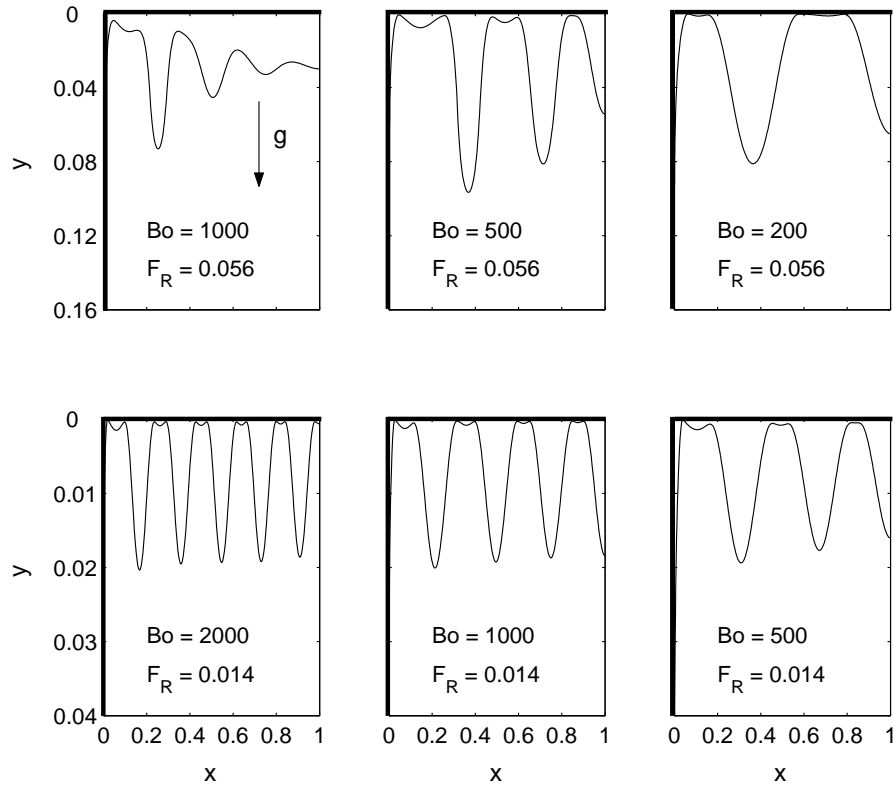


FIGURE 10. Formation of steady-state pendant drops. $F_R = 0.056$ and 0.014 correspond to $\epsilon = 0.01$ and 0.002 , respectively. The solid wall is indicated by a thick line. Only a portion of the vertical axis is shown. The initial and boundary conditions are as in figure 4.

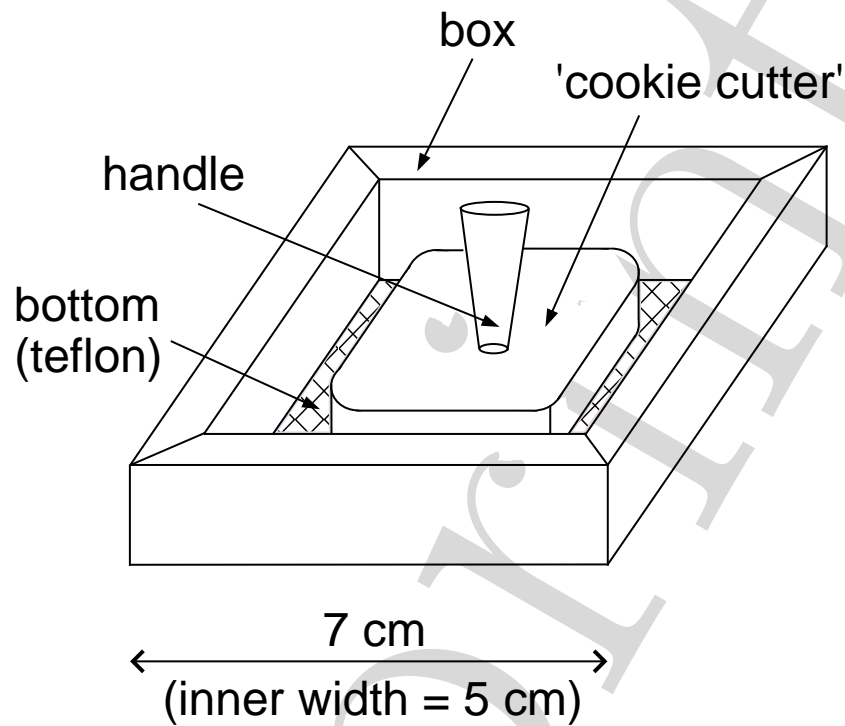


FIGURE 11. Schematic of the experimental device. Not to scale. The square box is made out of Plexiglas and a solution of water and glycerol is injected in the gap — shown as a shaded region — between the box and the 'cookie-cutter'. The experiment consists of lifting the 'cookie-cutter' and observing how the fluid evolves under surface tension. In a second set of experiments the box is tilted to investigate the effect of gravity. No 'cookie-cutter' is used in this case.

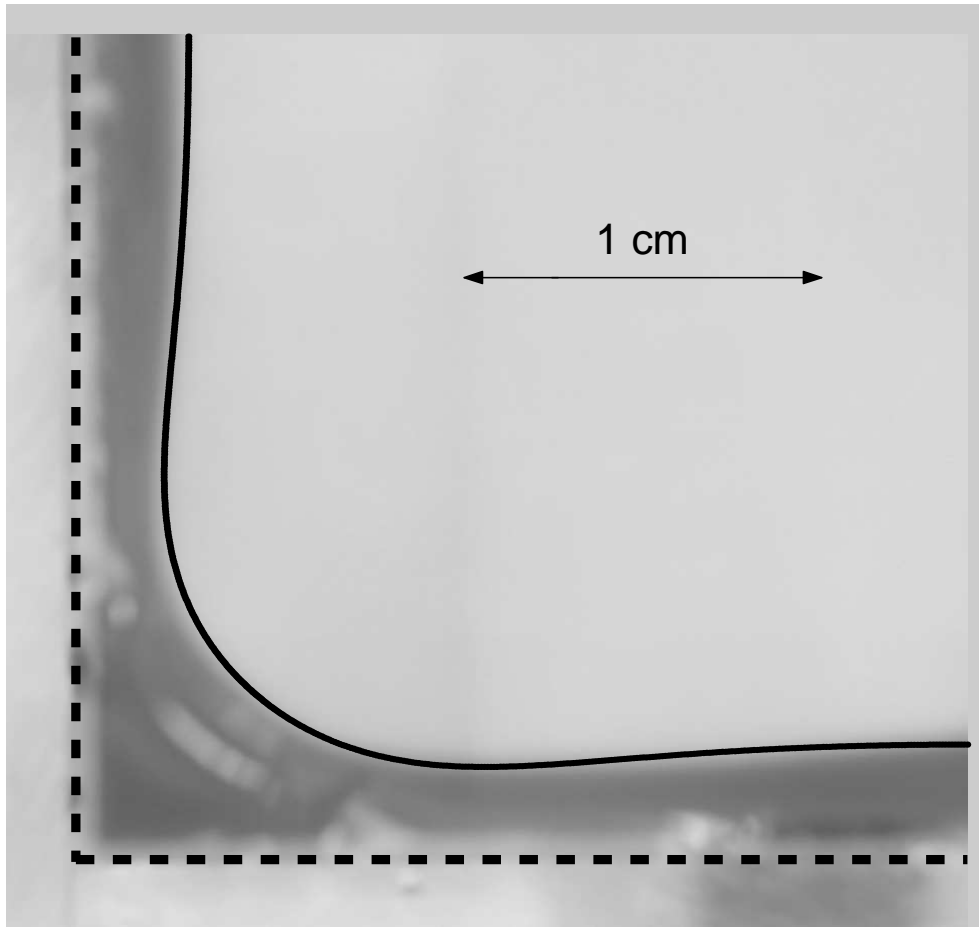


FIGURE 12. The steady state of a thin film governed by surface tension ($Bo = 0$): model prediction (thick line) versus experimental result (background picture). The filling fraction is $F_R = 0.19$ ($\epsilon = 0.047$). The dashed line indicates the position of the walls of the box. Note that the steady state is different from the one in figure 4 due to three-dimensional effects. The initial and boundary conditions for the simulation are as in figure 4.

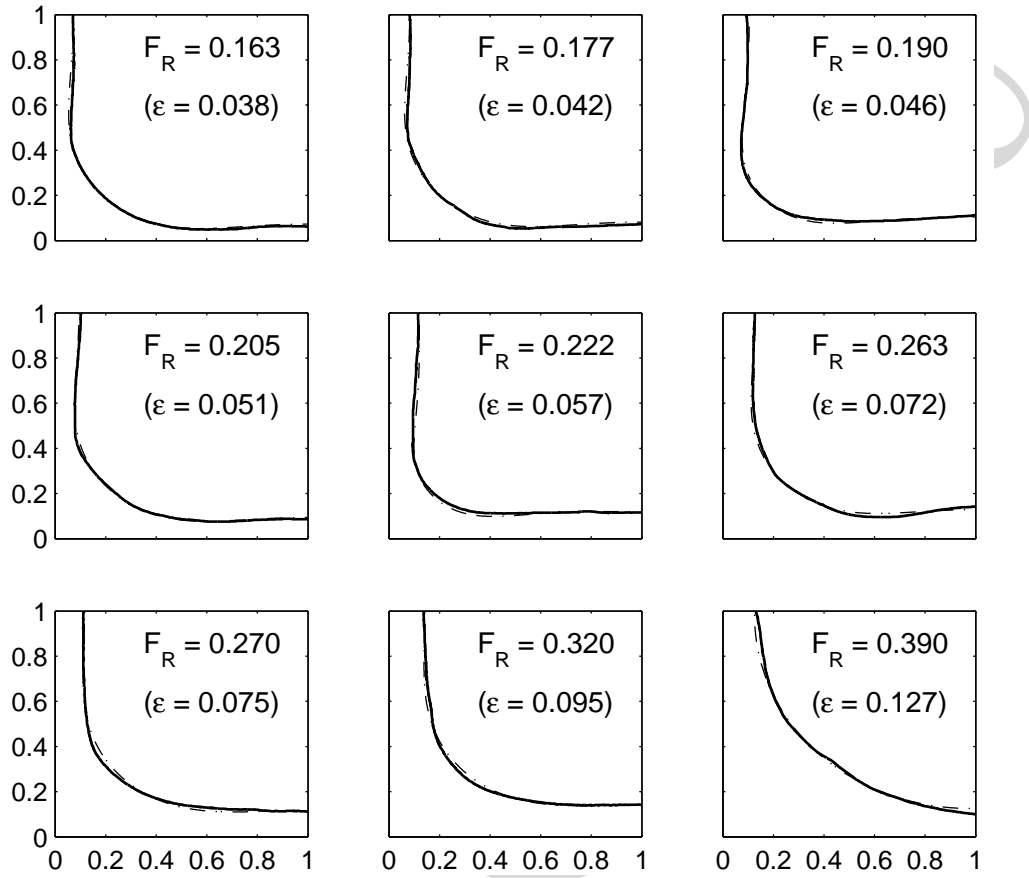


FIGURE 13. The steady state of a thin film governed by surface tension ($Bo = 0$) for several values of F_R : model predictions (dash-dotted line) versus experimental results (solid line). The two lines are almost everywhere on top of each other, indicating a striking agreement between theory and experiments. The interface for the experiments was reconstructed digitally as explained in the text. The initial and boundary conditions for the simulations are as in figure 4.

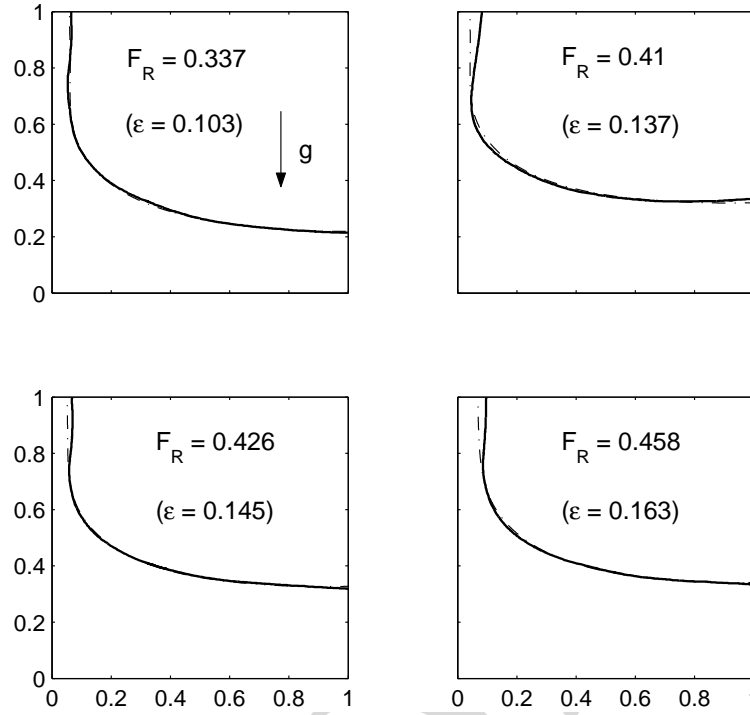


FIGURE 14. The steady state of a thin film governed by surface tension and gravity ($Bo = 15$) for four values of F_R : model predictions (dash-dotted line) versus experimental results (solid line). The two lines are almost everywhere on top of each other. Smaller filling fractions were difficult to obtain experimentally. The small discrepancy at the upper boundary is explained in the text. The steady state is different from the one in figure 8 due to three-dimensional effects, as explained in the text. The initial and boundary conditions for the simulations are as in figure 4.

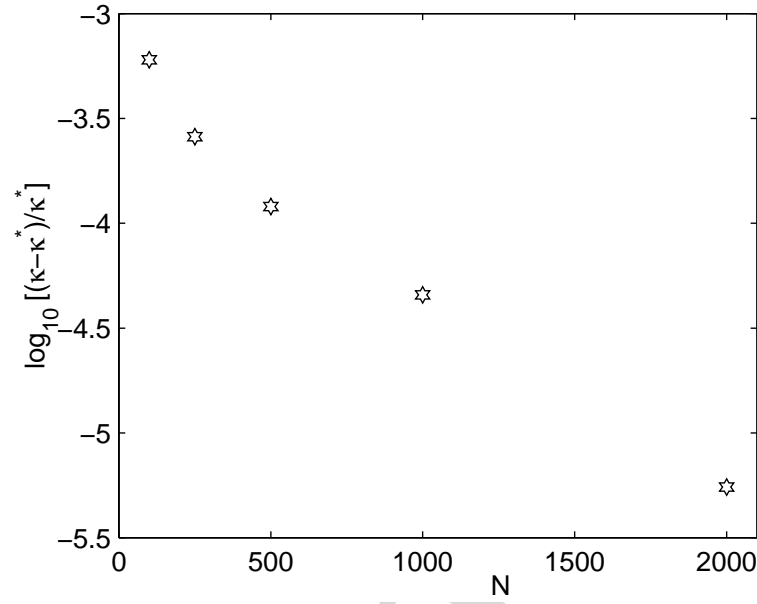


FIGURE 15. Relative error in the predicted steady-state curvature versus the number of grid points N for $Bo = 0$ and $F_R = 0.215$ ($\epsilon = 0.055$). κ is the curvature predicted from the model, κ^* is the theoretical curvature associated with the minimum surface configuration. The curvature from the model is computed as the average over $-0.5 \leq \xi \leq 0.5$.